

1 **Running head:**

2 Image-based plant disease phenotyping

3

4 **Author to whom all correspondence should be sent:**

5 Rebecca Bart

6 Donald Danforth Plant Science Center

7 975 North Warson Road

8 Saint Louis, MO 63132

9 Tel: 314-587-1696

10 Email: rbart@danforthcenter.org

11

12 **Research area:**

13 Ecophysiology and Sustainability

14

15

16

17

18

19

20

21

22

23

24

25

26

27

28

29

30

31

32 **Quantitative, image-based phenotyping methods provide insight into spatial and**
33 **temporal dimensions of plant disease**

34

35 Andrew M. Mutka^a, Sarah J. Fentress^a, Joel W. Sher^a, Jeffrey C. Berry^a, Chelsea Pretz^a,
36 Dmitri A. Nusinow^a and Rebecca Bart^{ab}

37

38 ^aDonald Danforth Plant Science Center, Saint Louis, MO

39

40 **Summary:**

41 Novel, image-based phenotyping methods enhance characterization of plant-pathogen
42 interactions.

43

44

45

46

47

48

49

50

51

52

53

54

55

56

57

58

59

60

61

62

63 **Footnotes:**

64 **Author contributions**

65 A.M.M. designed and performed experiments, analyzed data, and co-wrote the paper.
66 S.J.F. created bioluminescent bacterial strains, performed experiments, and edited the
67 paper. J.W.S. and C.P. performed experiments and provided technical assistance. J.C.B.
68 performed statistical analyses. D.A.N. co-supervised the development of the
69 bioluminescent imaging techniques and edited the paper. R.B. designed experiments,
70 supervised the study, and co-wrote the paper.

71

72 **Financial sources**

73 This work was supported by the Donald Danforth Plant Science Center.

74

75 ^b**Corresponding author: Rebecca Bart**

76 Email: rbart@danforthcenter.org

77

78

79

80

81

82

83

84

85

86

87

88

89

90

91

92

93

94 **Abstract**

95 Plant disease symptoms exhibit complex spatial and temporal patterns that are
96 challenging to quantify. Image-based phenotyping approaches enable multi-dimensional
97 characterization of host-microbe interactions and are well suited to capture spatial and
98 temporal data that are key to understanding disease progression. We applied image-based
99 methods to investigate cassava bacterial blight, which is caused by the pathogen
100 *Xanthomonas axonopodis* pv. *manihotis* (*Xam*). We generated *Xam* strains in which
101 individual predicted type III effector (T3E) genes were mutated and applied multiple
102 imaging approaches to investigate the role of these proteins in bacterial virulence.
103 Specifically, we quantified bacterial populations, water-soaking disease symptoms, and
104 pathogen spread from the site of inoculation over time for strains with mutations in
105 *avrBs2*, *xopX*, and *xopK* as compared to wild-type *Xam*. Δ *avrBs2* and Δ *xopX* both
106 showed reduced growth *in planta* and delayed spread through the vasculature system of
107 cassava. Δ *avrBs2* exhibited reduced water-soaking symptoms at the site of inoculation. In
108 contrast, Δ *xopK* exhibited enhanced induction of disease symptoms at the site of
109 inoculation but reduced spread through the vasculature. Our results highlight the
110 importance of adopting a multi-pronged approach to plant disease phenotyping to more
111 fully understand the roles of T3Es in virulence. Finally, we demonstrate that the
112 approaches used in this study can be extended to many host-microbe systems and
113 increase the dimensions of phenotype that can be explored.

114

115

116

117

118

119

120

121

122

123

124

125

126 **Introduction**

127 Plant diseases are responsible for significant reductions in agricultural
128 productivity worldwide, and for many diseases, control strategies are not available
129 (Chakraborty and Newton, 2011). Elucidating the molecular mechanisms that govern
130 host-microbe interactions has a robust track record of leading to the development of new
131 and effective resistance strategies. For example, plant innate immunity employs several
132 tiers of receptors that, at least in some instances, can be transferred among species (Tai et
133 al., 1999; Zhao et al., 2005; Lacombe et al., 2010; Tripathi et al., 2014; Schoonbeek et al.,
134 2015). Similarly, molecular dissection of the mechanisms used by pathogens to induce
135 susceptibility has led to the development of biotechnology methods for blocking
136 pathogenesis (Li et al., 2012; Strauß et al., 2012; Boch et al., 2014). A more complete
137 understanding of the mechanisms used by plant pathogens to cause disease is likely to
138 lead to the development of additional strategies with potential for translation to the field.

139 Collectively, research conducted over the past few decades has revealed a
140 complicated web of crosstalk that forms our current multi-tiered model of plant-pathogen
141 interactions. Plant pattern recognition receptors (PRRs) initiate immune responses after
142 recognition of conserved microbial features, such as flagellin and EF-Tu for bacteria and
143 chitin for fungi (Macho and Zipfel, 2014). Successful pathogens have evolved effector
144 proteins to suppress defenses and induce susceptibility within their hosts (Win et al.,
145 2012). Resistant hosts may recognize these effectors or their action to trigger robust
146 immune responses (Stam et al., 2014; Khan et al., 2016). Type III effectors (T3Es)
147 secreted into host cells by Gram-negative bacteria are among the most intensely studied
148 pathogen effector proteins, and yet, the function of most T3Es remains unknown.
149 Members of the *Xanthomonas* and *Pseudomonas* genera are among the most common
150 bacterial disease-causing agents and are known to have large and variable effector
151 repertoires (White et al., 2009; Lindeberg et al., 2012; Schornack et al., 2013). Efforts to
152 deduce the role of individual T3Es in bacterial virulence through characterization of
153 effector knockouts have concluded that while collectively important, many individual
154 effectors do not contribute substantially to virulence (Castañeda et al., 2005; Kvitko et
155 al., 2009; Cunnac et al., 2011; Dunger et al., 2012; Xie et al., 2012).

156 Advances in DNA sequencing technologies have provided a wealth of genomic
157 resources for bacterial species. Using genomics data generated from pathogenic bacteria,
158 we are able to predict T3E repertoires, and the function of individual effectors can then
159 be investigated with genetic knockouts (Baltrus et al., 2011; Bart et al., 2012; Roux et al.,
160 2015; Wei et al., 2015; Teper et al., 2016). Traditional plant disease phenotyping methods
161 have relied on visual assessment of symptoms (Bock et al., 2010) and quantification of
162 pathogen growth in host tissue (Whalen et al., 1991; Tornero and Dangl, 2001; Liu et al.,
163 2015). Visual inspection and scoring of symptoms are likely to be translatable to disease
164 progression within field settings. Inspection and scoring, however, are subject to surveyor
165 bias and may not capture subtle differences in disease severity (Poland and Nelson,
166 2011). Quantification of pathogen growth is a tractable system for comparison, but fails
167 to provide information regarding the complex spatial patterns of diseases that progress
168 over time. Thus, genetic studies of T3E mutants have likely missed phenotypes that are
169 difficult to measure with traditional methods, and new approaches are needed for
170 exploring additional dimensions of disease phenotypes.

171 High-throughput, image-based phenotyping methods are revolutionizing many
172 areas of plant biology research (Furbank and Tester, 2011; Fiorani and Schurr, 2013;
173 Araus and Cairns, 2014; Granier and Vile, 2014; Fahlgren et al., 2015; Zaman-Allah et
174 al., 2015). Analysis of plant phenotypes, such as size, shape, color, growth, and leaf area
175 altered by herbivory, can be automatically extracted from image data to observe how
176 such traits change over time (Green et al., 2012; Lamari, 2008). Image-based methods are
177 well suited to characterize the spatial and temporal dimensions of disease symptoms and
178 have been applied to several host-pathogen systems (Mahlein et al., 2012; Rousseau et
179 al., 2013; Bauriegel and Herppich, 2014; Baranowski et al., 2015; Li et al., 2015; Raza et
180 al., 2015). These studies illustrate the range of imaging data that can be generated to
181 automate and quantify detection of disease symptoms. Additionally, these studies
182 emphasize that each imaging assay must be calibrated to detect the critical aspects of the
183 pathosystem being studied.

184 Cassava (*Manihot esculenta*) is a major staple crop for an estimated 800 million
185 people in Africa, South America, and Asia (FAO, 2013) and is prized as a drought-
186 tolerant plant that is able to thrive on marginal lands. Among the diseases that impact this

187 crop is cassava bacterial blight (CBB), which is caused by the Gram-negative bacterial
188 pathogen *Xanthomonas axonopodis* pv. *manihotis* (*Xam*). CBB disease symptoms are
189 characterized at early stages by water-soaked lesions on leaves and at later stages of
190 infection by wilting and defoliation (Lozano, 1986). Currently, no disease resistance
191 genes have been demonstrated to be effective against CBB, and chemical methods are not
192 an economically feasible form of control for smallholder farmers. Consequently, novel,
193 genetically encoded methods of achieving plant immunity to CBB must be developed.
194 T3Es that are both conserved in *Xam* populations and important for virulence represent
195 possible targets for engineering durable resistance. Previously, the T3E repertoires for 65
196 *Xam* strains were predicted based on their genomic sequences (Bart et al., 2012). This
197 study predicted 13 to 23 effectors in each strain based on homology to proteins from
198 other systems, excluding the transcriptional activator-like (TAL) effectors that are not
199 resolved by Illumina short read technology. Currently, only a few TAL effectors have
200 been functionally characterized in *Xam* (Castiblanco et al., 2013; Cohn et al., 2014).
201 Notably, several recent studies have explored the use of alternate assays to elucidate the
202 role of T3Es in pathogen virulence (Castiblanco et al., 2013; Cernadas et al., 2014; Cohn
203 et al., 2014).

204 For this study, we focused on homologs of two previously characterized T3Es,
205 AvrBs2 and XopX, and one predicted T3E, XopK, whose role in virulence is unclear.
206 AvrBs2 contains a glycerol phosphodiesterase domain that is required for its virulence
207 functions in other *Xanthomonas* pathovars (Kearney and Staskawicz, 1990; Tai et al.,
208 1999; Zhao et al., 2011; Li et al., 2015). XopX is involved in suppressing pathogen-
209 triggered immunity (Metz et al., 2005; Sinha et al., 2013; Stork et al., 2015). XopK was
210 first identified in the rice pathogen *Xanthomonas oryzae* pv. *oryzae* (*Xoo*) (Furutani et al.,
211 2006). Previous data indicated that XopK is secreted through the type III secretion system
212 (T3SS) into host cells (Furutani et al., 2009; Schulze et al., 2012). Although the *xopK*
213 gene is conserved in many *Xanthomonas* species, its role in virulence is unknown
214 (Bogdanove et al., 2011; Potnis et al., 2011; Bart et al., 2012; Schulze et al., 2012;
215 Arrieta-Ortiz et al., 2013; Jalan et al., 2013).

216 Our efforts to phenotypically characterize these *Xam* mutants began with standard
217 methods such as visual monitoring of symptom development and quantifying bacterial

218 growth *in planta* over the course of several days. These methods were limited in
219 resolution, consistency between experiments, and robustness. Consequently, we sought to
220 apply image-based phenotyping methods to study this pathosystem. The first method
221 addresses issues of human bias during scoring by using a low-cost, Raspberry Pi
222 computer and camera to capture and quantify infection over time. The second approach
223 leverages a bioluminescent reporter system within the bacteria to non-invasively monitor
224 pathogen spread throughout the plant (Meyer et al., 2005; Xu et al., 2010). The
225 combination of these methods achieved unprecedented resolution and sensitivity for
226 quantifying the spatial and temporal dynamics of disease progression within the
227 laboratory setting. The results of this study highlight the importance of adopting a holistic
228 approach to phenotyping plant-pathogen interactions to reveal biological functions of
229 virulence proteins and inform development of disease control strategies.

230

231 **Results**

232 *Pathogen growth levels and symptom development for Xam type III effector mutants*

233 To investigate the virulence functions of predicted *Xam* T3Es, we generated
234 mutations in genes homologous to *avrBs2*, *xopX*, and *xopK*. Full gene deletions were
235 created by homologous recombination and initial analysis of pathogen growth levels and
236 symptom development were performed using standard methods (see Materials and
237 Methods) (Whalen et al., 1991; Liu et al., 2015). When inoculated by syringe infiltration
238 in a cassava leaf, wild-type *Xam* populations increased to high levels and caused dark
239 water-soaking symptoms that developed within days of inoculation (Fig. 1). In contrast,
240 mutation of the *hrpF* gene, which encodes a translocon protein required for type III
241 secretion (Buttner et al., 2002), caused a 2-log reduction in pathogen growth levels (Fig.
242 1, A-B) relative to the wild-type strain and eliminated water-soaking disease symptoms
243 (Fig. 1C). For the $\Delta avrBs2$ and $\Delta xopX$ mutants, we observed slightly decreased growth
244 levels compared with wild-type over a total of four independent experiments (Fig. 1A,
245 Supplemental Fig. S1). A generalized linear mixed model (GLMM) adjusted by
246 experiment and technical replicates indicated significant differences in pathogen growth
247 at 5 days post inoculation (dpi) for the $\Delta hrpF$ ($p < 0.001$, $\alpha = 0.05$), $\Delta avrBs2$ ($p < 0.001$,
248 $\alpha = 0.05$), and $\Delta xopX$ mutants ($p = 0.0155$, $\alpha = 0.05$), relative to wild-type. At 6 dpi, the

249 $\Delta avrBs2$ mutant exhibited a reduction in disease symptoms (Fig. 1C). There were no
250 obvious differences, however, in disease symptom production between the $\Delta xopX$ mutant
251 and wild-type at 6 dpi (Fig. 1C).

252 In contrast to the $\Delta avrBs2$ and $\Delta xopX$ mutants, we observed that the $\Delta xopK$
253 mutant exhibited pathogen growth levels that were either similar to or elevated compared
254 to wild-type across four experiments (Fig. 1B, Supplemental Fig. S1). A GLMM
255 indicated the growth differences observed for the $\Delta xopK$ mutant at 5 dpi were not
256 significantly different from wild-type ($p = 0.655$, $\alpha = 0.05$). However, water-soaking
257 disease symptoms caused by the $\Delta xopK$ mutant appeared enhanced at 6 dpi (Fig. 1C). To
258 address the limitations of visual assessment of disease and to better understand the
259 temporal dimension of this phenotype, we sought to develop a quantitative method of
260 assessing symptom development with increased time resolution.

261

262 *Image-based quantification of disease symptom development*

263 To develop a low-cost imaging system for semi-automated quantification of
264 disease symptom development, we used Raspberry Pi microcomputers and camera boards
265 to image the abaxial side of the leaf during symptom development (Fig. 2A). Following
266 data collection, regions of interest (ROI) were selected manually from the image stacks
267 that contained each inoculated spot, and image analysis was performed using an ImageJ
268 macro script (Fig. 2A, Supplemental Fig. S2).

269 We quantified water-soaking disease symptoms caused by wild-type *Xam*, along
270 with the $\Delta xopK$ and the $\Delta hrpF$ mutants (Fig. 2B). For the wild-type strain, disease
271 symptoms began appearing at approximately 100 hours post inoculation. As expected, the
272 $\Delta hrpF$ mutant did not produce disease symptoms throughout the course of the
273 experiment. For the $\Delta xopK$ mutant, an increased rate of symptom accumulation was
274 observed relative to the wild-type strain in the initial phase of disease appearance over
275 four separate experiments (Fig. 2B, Supplemental Fig. S3). To compare the rates of
276 symptom accumulation for these strains, we performed a GLMM analysis, adjusted by
277 experiment and technical replicates. Additionally, we adjusted for heteroskedasticity by
278 allowing the variance to be exponentially related to time. This analysis indicated that
279 slopes for both the $\Delta hrpF$ ($p < 0.0001$, $\alpha = 0.05$) and $\Delta xopK$ ($p = 0.0476$, $\alpha = 0.05$)

280 mutants were significantly different from wild-type. Thus, despite being a predicted T3E,
281 mutation of the *xopK* gene induces disease symptoms more rapidly during infection than
282 wild-type *Xam*.

283 To further investigate the impacts of other T3E mutations on disease symptom
284 progression, we performed imaging of cassava leaves inoculated with the *Xam* Δ *avrBs2*
285 and Δ *xopX* mutants (Fig. 2C, D). As with the experiments involving the Δ *xopK* mutant,
286 we used GLMM, adjusted by experiment, technical replicates, and heteroskedasticity.
287 The Δ *avrBs2* mutant exhibited significantly decreased disease symptom progression
288 relative to wild-type ($p < 0.0001$, $\alpha = 0.05$), consistent with visual observations of disease
289 (Fig 1). For the Δ *xopX* mutant, while symptom progression appeared slightly delayed
290 compared to wild-type, this effect was not significantly different from wild-type across
291 all experiments ($p = 0.1447$, $\alpha = 0.05$). Thus, in the T3E repertoire of *Xam*, AvrBs2 has a
292 greater contribution to early symptom progression than XopX.

293

294 *Characterizing bacterial spread in host tissue*

295 To observe the ability of T3E mutants to spread systemically during infection, we
296 developed a method to track bacterial spread *in planta*. This is particularly important for
297 *Xam* because it spreads through the host vascular system to cause disease (Lozano, 1986).
298 Therefore, bacterial growth and symptom development at the site of inoculation are
299 descriptive of only a small part of pathogenesis. It has been shown that bioluminescent
300 bacterial strains can be used to detect pathogen presence in host tissue (Bogs et al., 1998;
301 Meyer et al., 2005; Xu et al., 2010).

302 To determine if we could detect *Xam* and visualize spread from an initial infection
303 site *in planta*, we generated bioluminescent strains by introducing a plasmid driving
304 constitutive expression of the LUX operon into *Xam* and the T3E mutants by conjugation.
305 The inoculated areas were imaged in a dark chamber to detect the bioluminescence signal
306 after syringe inoculation of LUX strains into cassava leaves. Local areas infiltrated with
307 wild-type *Xam* exhibited a circular region of bioluminescence that appeared by 4 dpi,
308 followed by spread into surrounding tissues (Fig. 3). This spread extended beyond the
309 visible area of water-soaking symptoms observed at 9 dpi. These results indicate *Xam*
310 proliferates locally at the site of inoculation before invading into the nearby vasculature,

311 and that bacterial spread can be observed in regions of the plant that do not yet exhibit
312 visible symptoms.

313 To quantify the changes in bacterial luminescence observed from these images,
314 we applied image analysis methods for measuring both the convex hull area and
315 maximum span across the convex hull, which estimate the total area invaded and the
316 maximum linear distance of spread by the pathogen, respectively. Compared to wild-type
317 *Xam*, the $\Delta xopX$ mutant exhibited reduced spread, observed in five independent
318 experiments (Fig. 3, Supplemental Fig. S4). A GLMM, adjusted by experiment and
319 technical replicates, indicated at 9 dpi this reduction in spread quantified by convex hull
320 area was statistically significant ($p < 0.0001$, $\alpha = 0.05$). We observed significant
321 reduction in pathogen spread for the $\Delta avrBs2$ ($p = 0.0388$, $\alpha = 0.05$) and $\Delta xopK$ mutants
322 ($p = 0.0257$, $\alpha = 0.05$). Further consideration of these data revealed that experimental
323 noise reflected the timing of pathogen entry into the plant vasculature (Fig. 3,
324 Supplemental Fig. S4). These results highlight the importance of invasion into host
325 vasculature by *Xam* for virulence and the power of image-based phenotyping assays for
326 visualizing this dynamic process.

327

328 *Characterizing bacterial spread in vitro*

329 Given the phenotype observed for reduced spread in host tissue, next we
330 examined if any of the T3E mutants affected motility *in vitro* (Supplemental Fig. S5).
331 Bacteria were plated at the center of soft agar plates, which allowed them to spread across
332 the surface of the media (Lee et al., 2003; Tian et al., 2015). Using a Raspberry Pi-
333 controlled camera, images of the plates were taken for several days, and the area of
334 bacterial spread was quantified (Supplemental Fig. S5). We observed that the $\Delta hrpF$,
335 $\Delta avrBs2$, $\Delta xopX$, and $\Delta xopK$ mutants do not have any apparent motility defects on soft
336 agar. These results suggest that observed defects in mutant movement through host
337 vascular tissue are due to factors other than intrinsic bacterial motility.

338

339 *Imaging bacterial colonization in other pathosystems*

340 Since tracking bacterial colonization with a bioluminescent reporter was
341 successful in cassava, we wanted to expand the use of this method to other pathosystems.

342 To explore this, we generated bioluminescent *Xanthomonas campestris* pv. *campestris*
343 (*Xcc*) and *Xanthomonas euvesicatoria* (*Xe*) by conjugation. Following syringe inoculation
344 of bioluminescent *Xam* and *Xcc*, bacteria can be visualized near the site of infection and,
345 in the case of *Xam*, at distal sites following spread into the vasculature (Fig. 4). Since *Xe*
346 infection in pepper and tomato results in leaf spot disease, dip inoculations were used for
347 this strain to mimic field infections. Bioluminescent *Xe* could be readily detected in
348 distinct puncta across the leaf following dip inoculation (Fig. 4). These results
349 demonstrate the utility of bioluminescent technologies to track pathogens in diverse crop
350 plants.

351

352 **Discussion**

353 In complex interactions between hosts and pathogens, T3Es are key targets for
354 resistance strategies. The specific virulence functions of T3Es, however, can be difficult
355 to determine, and their characterization remains a primary goal of researchers within the
356 plant-microbe interaction field. Traditionally, relative virulence of pathogen strains is
357 quantified through visual assessment of plant symptoms and destructive harvesting to
358 measure pathogen populations over time. However, these methods alone often do not
359 provide enough information to make conclusions about T3E functions during infection.
360 Furthermore, CBB has a number of challenges for experimental study. For example, *Xam*
361 is able to spread *in planta* through both mesophyll and vascular tissue (Boher and
362 Verdier, 1994). The pattern of colonization for these distinct tissue types likely
363 contributes to observed experimental noise. Furthermore, cassava plants are propagated
364 from vegetative cuttings, so it is difficult to obtain plants that are developmentally
365 synchronized and physiological aspects of cassava plants such as latex content of leaves
366 may vary from one experiment to another. Finally, it is notable that cassava is a field
367 grown crop with a long generation time (12 months) and development of phenotyping
368 methods from which observations will translate to field setting is desirable.

369 To address these limitations, we applied image-based phenotyping methods that
370 enable quantification of spatial and temporal dynamics for plant-pathogen interactions
371 (Figure 5). Measuring symptom area with increased time resolution, enabled by
372 automated imaging, allowed us to observe an enhanced rate of early disease accumulation

373 for the $\Delta xopK$ mutant. This phenotype demonstrates the importance of a pathogen's
374 ability to establish infection for overall virulence. While XopK is a predicted T3E
375 effector that carries the hallmarks of a secreted virulence factor (Furutani et al., 2006;
376 Furutani et al., 2009; Schulze et al., 2012), its roles during infection appear to be
377 complex. The XopK protein sequence contains 54% hydrophobic residues and several
378 predicted transmembrane domains. Thus, it is possible this protein is associated with host
379 cell membranes following secretion. Our observations for XopK are contrasted with the
380 roles of AvrBs2 and XopX, which exhibit reduced virulence phenotypes, consistent with
381 previous studies (Kearney and Staskawicz, 1990; Metz et al., 2005; Zhao et al., 2011;
382 Sinha et al., 2013; Li et al., 2015; Stork et al., 2015). Our results further illustrate that
383 T3E mutants may impact certain aspects of host-pathogen interactions more than others.
384 For example, XopX contributes more to *Xam* proliferation in the host than to disease
385 symptom progression, while AvrBs2 contributes significantly to both aspects of infection.
386 Thus, combining data from several phenotyping approaches is necessary for determining
387 the roles of T3Es in virulence (Table 1).

388 Another challenge of studying plant-pathogen interactions is visualizing and
389 quantifying a pathogen's location and movement in host tissue. As we observed imaging
390 *Xam* strains in cassava, bioluminescence is a powerful tool for studying the spatial and
391 temporal dimensions of pathogen spread in host tissue. Previously, bioluminescent
392 bacterial strains were used to visualize *Xcc* infection in *Arabidopsis thaliana* (Meyer et
393 al., 2005). Also bioluminescent strains of the tomato pathogen *Clavibacter michiganensis*
394 were used to track bacterial movement following grafting and during germination (Xu et
395 al., 2010). Imaging of bioluminescence with increased spatial resolution allows for
396 quantification of patterns of pathogen spread, as we observed for *Xam* infection in
397 cassava leaves. Our studies visualized the process by which *Xam* invades host
398 vasculature. The experimental variation we observed suggests this is a dynamic process
399 impacted by a range of factors, such as proximity to primary and secondary leaf veins,
400 leaf developmental status, and environmental conditions. These variables can be
401 investigated using our imaging approaches. In particular, environmental factors such as
402 humidity and heat are known to be important for CBB severity in the field (Boher and
403 Verdier, 1994). How these conditions promote disease severity is currently unknown but

404 may be related to mechanisms of pathogen spread in host tissue. These factors can be
405 readily explored by direct imaging using an environmentally controlled chamber.

406 While image-based phenotyping approaches offer great promise, characterizing
407 plant-pathogen interactions with such methods also has many challenges, in part due to
408 the diverse range of symptoms and multiple scales at which disease occurs. For each
409 pathosystem, one must first identify the relevant aspects of the infection that can be
410 imaged and the relevant metrics that are needed to characterize the system. This initial
411 study relied on visible light imaging. In future studies, other wavelengths of the
412 electromagnetic spectrum that provide additional information for characterizing disease
413 will be considered. Hyperspectral imaging, which collects spectral data for every pixel,
414 has been used to classify and quantify several diseases that infect sugar beet (Mahlein et
415 al., 2012; Leucker et al., 2016). Thermal imaging offers another approach for detecting
416 disease in plant canopies, since many diseases impact transpiration rates and, therefore,
417 plant surface temperature. While environmental variation can introduce challenges into
418 thermal imaging, Raza et al. addressed this issue by using a combination of thermal and
419 visible light imaging, along with depth estimation, to detect diseased tomato plants using
420 a machine learning approach (Raza et al., 2015). In a laboratory context, fine-scale
421 imaging of disease symptoms on a single leaf may be the optimal approach for
422 investigating certain experimental questions, while whole-plant or field-scale imaging
423 would be necessary for detecting disease in an agricultural context. Unmanned aerial
424 vehicles performing multispectral imaging were used at the field scale to examine abiotic
425 stress in maize (Zaman-Allah et al., 2015). Biotic stresses likely could be detected using
426 similar signatures from aerial imaging.

427 This study presents a new approach to investigation of plant-pathogen
428 interactions. Inspired by the advances of image-based phenotyping methods in other areas
429 of plant biology, we have applied similar methods to quantifying spatial and temporal
430 dimensions of disease development. This approach expands the potential range of
431 phenotypes that can be explored, enabling insights that are difficult to obtain by
432 traditional methods. Since many smallholder farmers in the developing world rely on
433 cassava for food security, low-cost monitoring devices that enable rapid detection of
434 disease outbreaks in the field would be beneficial. In an ideal scenario, monitoring

435 devices would be deployed to cassava fields in disease-prone regions and transmit data
436 over wireless networks to give farmers early warning of disease outbreaks. Many
437 technical and logistical challenges would need to be overcome to achieve this goal.
438 However, our image-based methods for detecting disease represent a first step in
439 developing capabilities for such a device. Remote detection of disease through imaging
440 or other means is a promising approach for plant pathology research that can be translated
441 from the laboratory to the field. While characterizing each plant-pathogen system has its
442 own unique challenges, image-based phenotyping methods can be adapted for many
443 systems and offer the potential to revolutionize plant disease identification and
444 quantification.

445

446 **Materials and methods**

447 *Bacterial strains and plant varieties*

448 The following strains of *Xanthomonas axonopodis* pv. *manihotis* (*Xam*) were used:
449 *Xam668*, *Xam668* Δ *avrBs2*, *Xam668* Δ *hrpF*, *Xam668* Δ *xopK*, and *Xam668* Δ *xopX*. For
450 experiments performed in cassava (*Manihot esculenta*), variety 60444 was used, except
451 in experiments noted where variety TME7 was used. Strains used for other pathosystems
452 include: *Xanthomonas euvesicatoria* (*Xe* 85-10) and *Xanthomonas campestris* pv.
453 *campestris* (*Xcc* 8004). For experiments in pepper, *Capsicum annuum* variety ECW was
454 used. For experiments in tomato, *Solanum lycopersicum* variety M82 was used. For
455 experiments in broccoli, *Brassica oleracea*, was used.

456

457 *Generation of bacterial mutants*

458 To generate gene deletion mutants in bacteria, we used a homologous
459 recombination strategy, in which genomic regions flanking each gene of interest were
460 first cloned into the pENTR-d-TOPO vector (Invitrogen). Blunt-end cloning of the PCR
461 products was performed to introduce the PCR fragments into pENTR-d-TOPO.
462 Restriction sites added with the primers were used to create a version of the vector with 5'
463 and 3' flanking regions adjacent to each other. Gateway cloning was used to transfer this
464 cassette into the pLVC18-sacBR vector, which enabled a sucrose counter-selection
465 approach to be used in creating unmarked gene deletions (Logue et al., 2009). This vector

466 was conjugated into *Xam* using a triparental mating system, with an *E. coli* helper strain
467 containing the pRK600 plasmid. Mutants with the unmarked gene knockout were
468 confirmed with PCR.

469

470 *Bacterial inoculations and growth monitoring in planta*

471 To quantify bacterial growth in plant tissue, leaves were inoculated with solutions
472 of bacterial strains ($OD_{600} = 0.0001$) re-suspended in 10 mM $MgCl_2$. Prior to inoculation,
473 the leaf was wounded with a razor blade, and the bacterial solutions were injected into the
474 leaf with a needleless 1-mL syringe. Approximately 0.1 mL of bacterial solution was
475 injected at each inoculation site.

476 For each time point that bacterial growth was monitored, leaf punches were taken
477 from inoculated regions. A 1-cm diameter cork borer was used to excise a leaf disk,
478 which was then ground with a tungsten carbide bead in 200 μL of 10 mM $MgCl_2$ using a
479 TissueLyser (Qiagen). Dilutions of the leaf lysate were then plated on NYG agar media
480 with 100 $\mu g \mu L^{-1}$ rifampicin, and *Xam* colonies were counted to estimate the number of
481 bacteria in the original leaf sample.

482

483 *Image acquisition and analysis for quantification of disease symptoms*

484 Leaves were inoculated with solutions of bacterial strains ($OD_{600} = 0.001$). The
485 leaves were then taped to a black surface, such that the abaxial side of the leaf faced
486 downward toward a camera. Images of disease symptoms were taken with Raspberry Pi
487 5MP camera boards controlled by Raspberry Pi Model B microcomputers. Hourly
488 automated image collection was done with Cron. For all experiments shown, images were
489 taken hourly. Image stacks were analyzed with FIJI, running ImageJ version 2.0.0-rc-
490 30/1.49v (Schindelin et al., 2012; Schindelin et al., 2015). The scale of the image stacks
491 was determined with a ruler included in the image, enabling unit conversion from pixels
492 to cm.

493 A region of interest (ROI) was selected that contained each inoculated area. An
494 ImageJ macro script was used to select and quantify the area of water-soaking symptoms
495 for each ROI (Supplemental File S1). The ROI stacks were converted to HSB (hue-
496 saturation-brightness) color space. After selecting the saturation channel, a background

497 subtraction was performed. Then, the area of disease was selected by creating a binary
498 image with black pixels representing symptomatic regions and white pixels representing
499 non-symptomatic tissue. The binary images were created by applying a threshold
500 calculated by the following,

$$t = \mu - n\sigma$$

501 where t = threshold, μ = mean saturation value of the ROI stack, and σ = standard
502 deviation of saturation values for the ROI stack. For the variable n , a range of values
503 were tested to determine the appropriate threshold for selecting disease symptoms. The
504 area of black pixels in the binary images was then quantified to determine the area of
505 disease symptoms for each ROI.

506

507 *Bioluminescence imaging and analysis*

508 Bioluminescent bacteria were generated by conjugating the pLUX plasmid into
509 *Xanthomonas* strains of interest. Leaves were inoculated with solutions of these strains
510 ($OD_{600} = 0.01$), with one strain inoculated per leaf lobe. Images were taken using a Star I
511 CCD digital camera system (Photometrics Ltd.) or a PIXIS 1024B (Princeton
512 Instruments) that was contained in a blackout chamber. The cameras were operated with
513 WinView/32 software version 2.5.22.0 (Princeton Instruments) or μ Manager v1.4.22
514 (Open Imaging), respectively.

515 Using ImageJ, each image was converted to an 8-bit TIFF file. Then, the Auto
516 Enhance Contrast function was applied, and a binary image was created with the Auto
517 Threshold function using the MaxEntropy algorithm (Kapur et al., 1985). Next, the
518 Despeckle and Invert functions were applied to create an image in which the
519 bioluminescent signal was represented by black pixels. Finally, the Hull and Circle plugin
520 v2.1b (<http://rsb.info.nih.gov/ij/plugins/hull-circle.html>) was used to select and quantify
521 the convex hull for each shape representing the bioluminescence signal.

522

523 *In vitro bacterial motility assays*

524 The ability of *Xam* strains to spread *in vitro* was observed on NYG media
525 containing 0.25% agar and $100 \mu\text{g } \mu\text{L}^{-1}$ rifampicin. $10 \mu\text{L}$ of a bacterial solution ($OD_{600} =$
526 0.1) was spotted in the center of each plate. A Raspberry Pi camera was set to image the

527 plates from a top-view. Images of the plates were taken over several days, as the bacteria
528 spread from the center of the plates. The ROI containing the bacterial colony on each
529 plate was selected, and an ImageJ macro script was used to create a binary image where
530 black pixels represented the area of the bacterial colony (Supplemental File S2). The
531 number of black pixels was then quantified to determine the bacterial area on the plate.

532

533 *Data and statistical analysis*

534 All graphs and data analyses were generated with R version 3.1.3 (R Core Team,
535 2015), using the following packages: ggplot2 version 1.0.1 (Wickham, 2009), knitr
536 version 1.11 (Xie, 2015), lme4 version 1.1-11 (Bates et al., 2015), lsmeans version 2.20-
537 23 (Lenth, 2015), multcomp version 1.4-4 (Hothorn et al., 2008), nlme version 3.1-128
538 (Pinheiro et al. 2016), plyr version 1.8.3 (Wickham, 2011), reshape2 version 1.4.1
539 (Wickham, 2007), and scales version 0.3.0 (Wickham, 2015). For each data set, a
540 generalized linear mixed model was used to assess the responses as a function of different
541 bacterial strains and over time while adjusting for correlation structures due to repeated
542 measures and cross-experimental variation. After the models were fit and checked for
543 underlying assumptions, statistical contrasts were implemented using a post hoc Tukey's
544 t test to compare the effect of interest across the different bacterial strains using an α level
545 of 0.05 as the cutoff for statistical significance.

546

547 **Supplemental material**

548 The following supplemental materials are available.

549

550 Supplemental Figure S1. Replicate experiments for analysis of *Xam* T3E mutant growth
551 *in planta* shown in Fig. 1.

552

553 Supplemental Figure S2. Image analysis optimization for water-soaking disease
554 symptoms caused by *Xam*.

555

556 Supplemental Figure S3. Replicate experiments for analysis of water-soaking symptoms
557 shown in Fig. 2.

558

559 Supplemental Figure S4. Replicate experiments for analysis of *Xam* spread in leaves
560 using bioluminescence imaging shown in Fig. 4.

561

562 Supplemental Figure S5. *In vitro* motility of *Xam* T3E mutants.

563

564 Supplemental File S1. ImageJ macro script used to quantify water-soaking disease
565 symptoms.

566

567 Supplemental File S2. ImageJ macro script used to quantify bacterial spread on soft agar
568 plates.

569

570 **Acknowledgments**

571 We would like to thank Malia Gehan and Noah Fahlgren for their help with the image
572 acquisition and analysis.

573

574 **Figure legends**

575 **Figure 1.** Disease symptom development and growth levels for *Xam* type III effector
576 (T3E) mutants in cassava. A-B, Growth levels of *Xam* wild-type, $\Delta hrpF$, $\Delta avrBs2$,
577 $\Delta xopX$, and $\Delta xopK$ mutants following syringe infiltration in leaves ($OD_{600} = 0.0001$).
578 Median, first and third quartiles are shown. The whiskers extend to the highest and lowest
579 data point falling within 1.5*IQR (inter-quartile range). Dots represent outliers that fall
580 outside 1.5*IQR. Each experiment was repeated three additional times (see Supplemental
581 Fig. S1). C, Comparison of disease symptoms caused by T3E mutants on leaves at 6 days
582 after syringe infiltration ($OD_{600} = 0.0001$). D, Results of generalized linear mixed model
583 analysis, combining bacterial growth data from all replicate experiments. Combined
584 estimated means and standard error (SE) are presented, as well as the difference between
585 the means and the p-values for each pairwise statistical contrast.

586

587 **Figure 2.** Quantification of disease symptoms caused by *Xam* on cassava leaves using
588 imaging. A, Illustration of the imaging set-up. Leaves were syringe infiltrated with

589 bacterial solutions ($OD_{600} = 0.001$) and taped to a black surface for imaging of the abaxial
590 side of the leaf. Raspberry Pi microcomputer with attached camera collected images once
591 per hour. Image analysis steps in ImageJ are shown and described in Materials and
592 Methods. The number of black pixels was quantified to determine the area of disease. B-
593 D, Quantification of water-soaking symptoms caused by the *Xam* wild-type strain and
594 three mutants over time. Dots represent individual measurements determined from image
595 analysis, and local regression fitted curves are plotted for each bacterial strain. Shaded
596 areas represent the 95% confidence interval for each curve. The experiment was repeated
597 three additional times with similar results (see Supplemental Fig. S3). E, Results of
598 generalized linear mixed model analysis, combining data from all replicate experiments.
599 Combined estimated slopes and standard error (SE) are presented, as well as p values for
600 each pairwise statistical contrast.

601

602 **Figure 3.** Bioluminescence imaging of *Xam* spread in cassava leaves. A, The
603 bioluminescence reporter pLUX plasmid was introduced into *Xam* strains. Leaves were
604 inoculated with bacterial solutions ($OD_{600} = 0.01$) using syringe infiltration. RGB images
605 of inoculated leaves reveal symptom development. Bioluminescence was visualized in a
606 dark chamber with a 5-10 min exposure. Image processing was performed with ImageJ to
607 select the area of bioluminescence and the convex hull of the resulting shapes were
608 analyzed. B, Representative quantification of convex hull for wildtype *Xam* and three
609 mutants. Additional replicate experiments are shown in Supplemental Fig. S4. C, Results
610 of generalized linear mixed model analysis of convex hull area, combining data from all
611 replicate experiments. Combined estimated means and standard error (SE) are presented,
612 as well as the difference between the means and the p-values for each pairwise statistical
613 contrast.

614

615 **Figure 4.** Comparison of vascular and leaf spot pathogens. *Xam* and *Xcc* were visualized
616 following syringe inoculation ($OD_{600} = 0.01$) at 18 days post inoculation (dpi) and 12 dpi,
617 respectively. Bacterial spot on pepper and tomato were visualized following dip
618 inoculation ($OD_{600} = 0.5$) of *Xe* at 9 dpi.

619

620 **Figure 5.** Summary for type III effector mutant phenotypes as revealed by different
621 phenotyping methods.

622

623 **Supplemental Figure S1.** Replicate experiments for analysis of *Xam* T3E mutant growth
624 *in planta* shown in Figure 1. A-C, Three additional experiments to quantify growth levels
625 of the *Xam* wild type strain, and the *Xam* $\Delta hrpF$, $\Delta avrBs2$, and $\Delta xopX$ mutants following
626 syringe infiltration in leaves ($OD_{600} = 0.0001$). D-F, Three additional experiments to
627 quantify growth levels of wild-type *Xam*, and the $\Delta hrpF$ and $\Delta xopK$ mutants following
628 syringe infiltration in leaves ($OD_{600} = 0.0001$).

629

630 **Supplemental Figure S2.** Image analysis optimization for water-soaking disease
631 symptoms caused by *Xam*. Following conversion of regions of interest (ROI) to hue-
632 saturation-brightness (HSB) color space and background subtraction, the distributions of
633 pixel values for each channel were examined. Disease symptoms are best represented by
634 pixel values in the lower tail of the distribution for the saturation channel. A range of
635 threshold values were applied to the images to create binary images, according to the
636 formula $t = \mu - n\sigma$, where t = threshold, μ = mean saturation value for the image stack,
637 and σ = standard deviation of saturation values for the image stack. Graphs show
638 example thresholds where $n = 3$ (blue line), $n = 2.5$ (red line), and $n = 2$ (green line). The
639 binary images on the right show the results of applying the $n = 3$ threshold.

640

641 **Supplemental Figure S3.** Three additional replicate experiments for analysis of water-
642 soaking symptoms shown in Fig. 2. Dots represent individual measurements determined
643 from image analysis, and local regression fitted curves are plotted for each bacterial
644 strain. Shaded areas represent the 95% confidence interval for each curve. For the
645 experiment shown in A, the image distances were not scaled to cm, so values are reported
646 in pixels. Experiments shown in panels D-F and H-I were performed with cassava variety
647 TME7.

648

649 **Supplemental Figure S4.** Replicate experiments for analysis of *Xam* spread in leaves
650 using bioluminescence imaging shown in Fig. 3. Three additional experiments

651 quantifying the convex hull area for the *Xam* $\Delta xopX$ (A-C), $\Delta avrBs2$ (D-F), and $\Delta xopK$
652 (G-I) mutants. Quantification of the maximum span across the convex hull for the same
653 experiments (K-S). Quantification of the convex hull area (T) and maximum span (U) for
654 a fourth replicate experiment including the three mutants. Dots represent individual
655 measurements; lines connect the mean at each time point. V, Results of generalized linear
656 mixed model analysis for maximum span results, combining data from all replicate
657 experiments. Combined estimated means and standard error (SE) are presented, as well as
658 p values for each pairwise statistical contrast.

659

660 **Supplemental Figure S5.** *In vitro* motility of *Xam* T3E mutants. Bacteria were spotted in
661 the center of plates containing NYG media with 0.25% agar. Images were taken of the
662 plates over several days, and the area of bacterial spread was quantified using ImageJ. A,
663 Example of binary thresholding used to select the area of bacterial spread from the
664 images. B-D, Quantification of bacterial spread for the *Xam* T3E mutants, relative to the
665 wild-type strain. Dots represent individual data points, and local regression fitted curves
666 are plotted for each bacterial strain. Shaded areas represent the 95% confidence interval
667 for each strain.

668

669 REFERENCES

670

- 671 Araus JL, Cairns JE (2014) Field high-throughput phenotyping: the new crop breeding
672 frontier. *Trends Plant Sci* 19: 52-61
- 673 Arrieta-Ortiz ML, Rodriguez RL, Perez-Quintero AL, Poulin L, Diaz AC, Arias Rojas N,
674 Trujillo C, Restrepo Benavides M, Bart R, Boch J, Boureau T, Darrasse A, David
675 P, Duge de Bernonville T, Fontanilla P, Gagnevin L, Guerin F, Jacques MA,
676 Lauber E, Lefeuvre P, Medina C, Medina E, Montenegro N, Munoz Bodnar A,
677 Noel LD, Ortiz Quinones JF, Osorio D, Pardo C, Patil PB, Poussier S, Pruvost O,
678 Robene-Soustrade I, Ryan RP, Tabima J, Urrego Morales OG, Verniere C,
679 Carrere S, Verdier V, Szurek B, Restrepo S, Lopez C, Koebnik R, Bernal A
680 (2013) Genomic survey of pathogenicity determinants and VNTR markers in the
681 cassava bacterial pathogen *Xanthomonas axonopodis* pv. *Manihotis* strain
682 CIO151. *PLOS One* 8: e79704
- 683 Baltrus DA, Nishimura MT, Romanchuk A, Chang JH, Mukhtar MS, Cherkis K, Roach J,
684 Grant SR, Jones CD, Dangl JL (2011) Dynamic evolution of pathogenicity
685 revealed by sequencing and comparative genomics of 19 *Pseudomonas syringae*
686 isolates. *PLOS Pathog* 7: e1002132

- 687 Baranowski P, Jedryczka M, Mazurek W, Babula-Skowronska D, Siedliska A,
688 Kaczmarek J (2015) Hyperspectral and thermal imaging of oilseed rape (*Brassica*
689 *napus*) response to fungal species of the genus *Alternaria*. PLOS One 10:
690 e0122913
- 691 Bart R, Cohn M, Kassen A, McCallum EJ, Shybut M, Petriello A, Krasileva K, Dahlbeck
692 D, Medina C, Alicai T, Kumar L, Moreira LM, Neto JR, Verdier V, Santana MA,
693 Kositcharoenkul N, Vanderschuren H, Gruissem W, Bernal A, Staskawicz BJ
694 (2012) High-throughput genomic sequencing of cassava bacterial blight strains
695 identifies conserved effectors to target for durable resistance. Proc Natl Acad Sci
696 USA 109: 13130-13130
- 697 Bates D, Maechler M, Bolker B, Walker S (2015) Fitting linear mixed-effects models
698 using lme4. J Stat Softw 67: 1-48
- 699 Bauriegel E, Herppich W (2014) Hyperspectral and chlorophyll fluorescence imaging for
700 early detection of plant diseases, with special reference to *Fusarium* spec.
701 infections on wheat. Agriculture 4: 32-57
- 702 Boch J, Bonas U, Lahaye T (2014) TAL effectors - pathogen strategies and plant
703 resistance engineering. New Phytol 204: 823-832
- 704 Bock CH, Poole GH, Parker PE, Gottwald TR (2010) Plant disease severity estimated
705 visually, by digital photography and image analysis, and by hyperspectral
706 imaging. Crit Rev Plant Sci 29: 59-107
- 707 Bogdanove AJ, Koebnik R, Lu H, Furutani A, Angiuoli SV, Patil PB, Van Sluys MA,
708 Ryan RP, Meyer DF, Han SW, Aparna G, Rajaram M, Delcher AL, Phillippy
709 AM, Puiu D, Schatz MC, Shumway M, Sommer DD, Trapnell C, Benahmed F,
710 Dimitrov G, Madupu R, Radune D, Sullivan S, Jha G, Ishihara H, Lee SW,
711 Pandey A, Sharma V, Sriariyanun M, Szurek B, Vera-Cruz CM, Dorman KS,
712 Ronald PC, Verdier V, Dow JM, Sonti RV, Tsuge S, Brendel VP, Rabinowicz
713 PD, Leach JE, White FF, Salzberg SL (2011) Two new complete genome
714 sequences offer insight into host and tissue specificity of plant pathogenic
715 *Xanthomonas* spp. J Bacteriol 193: 5450-5464
- 716 Bogs J, Bruchmüller I, Erbar C, Geider K (1998) Colonization of host plants by the fire
717 blight pathogen *Erwinia amylovora* marked with genes for bioluminescence and
718 fluorescence. Phytopathology 88: 416-421
- 719 Boher B, Verdier V (1994) Cassava bacterial blight in Africa: the state of knowledge and
720 implications for designing control strategies. Afr Crop Sci J 2: 505-509
- 721 Buttner D, Nennstiel D, Klusener B, Bonas U (2002) Functional analysis of HrpF, a
722 putative type III translocator protein from *Xanthomonas campestris* pv. *vesicatoria*.
723 J Bacteriol 184: 2389-2398
- 724 Castañeda A, Reddy JD, El-Yacoubi B, Gabriel DW (2005) Mutagenesis of all eight *avr*
725 genes in *Xanthomonas campestris* pv. *campestris* had no detected effect on
726 pathogenicity, but one *avr* gene affected race specificity. Mol Plant Microbe
727 Interact 18: 1306-1317
- 728 Castiblanco LF, Gil J, Rojas A, Osorio D, Gutierrez S, Munoz-Bodnar A, Perez-Quintero
729 AL, Koebnik R, Szurek B, Lopez C, Restrepo S, Verdier V, Bernal AJ (2013)
730 TALE1 from *Xanthomonas axonopodis* pv. *manihotis* acts as a transcriptional
731 activator in plant cells and is important for pathogenicity in cassava plants. Mol
732 Plant Pathol 14: 84-95

- 733 Cernadas RA, Doyle EL, Nino-Liu DO, Wilkins KE, Bancroft T, Wang L, Schmidt CL,
734 Caldo R, Yang B, White FF, Nettleton D, Wise RP, Bogdanove AJ (2014) Code-
735 assisted discovery of TAL effector targets in bacterial leaf streak of rice reveals
736 contrast with bacterial blight and a novel susceptibility gene. *PLOS Pathog* 10:
737 e1003972
- 738 Chakraborty S, Newton AC (2011) Climate change, plant diseases and food security: an
739 overview. *Plant Pathol* 60: 2-14
- 740 Cohn M, Bart RS, Shybut M, Dahlbeck D, Gomez M, Morbitzer R, Hou BH, Frommer
741 WB, Lahaye T, Staskawicz BJ (2014) *Xanthomonas axonopodis* virulence is
742 promoted by a transcription activator-like effector-mediated induction of a
743 SWEET sugar transporter in cassava. *Mol Plant Microbe Interact* 27: 1186-1198
- 744 Cunnac S, Chakravarthy S, Kvitko BH, Russell AB, Martin GB, Collmer A (2011)
745 Genetic disassembly and combinatorial reassembly identify a minimal functional
746 repertoire of type III effectors in *Pseudomonas syringae*. *Proc Natl Acad Sci USA*
747 108: 2975-2980
- 748 Dunger G, Garofalo CG, Gottig N, Garavaglia BS, Rosa MC, Farah CS, Orellano EG,
749 Ottado J (2012) Analysis of three *Xanthomonas axonopodis* pv. *citri* effector
750 proteins in pathogenicity and their interactions with host plant proteins. *Mol Plant*
751 *Pathol* 13: 865-876
- 752 Fahlgren N, Gehan MA, Baxter I (2015) Lights, camera, action: high-throughput plant
753 phenotyping is ready for a close-up. *Curr Opin Plant Biol* 24C: 93-99
- 754 FAO (2013) Save and grow: cassava. A guide to sustainable production intensification.
- 755 Fiorani F, Schurr U (2013) Future scenarios for plant phenotyping. *Annu Rev Plant Biol*
756 64: 267-291
- 757 Furbank RT, Tester M (2011) Phenomics--technologies to relieve the phenotyping
758 bottleneck. *Trends Plant Sci* 16: 635-644
- 759 Furutani A, Nakayama T, Ochiai H, Kaku H, Kubo Y, Tsuge S (2006) Identification of
760 novel HrpXo regulons preceded by two cis-acting elements, a plant-inducible
761 promoter box and a -10 box-like sequence, from the genome database of
762 *Xanthomonas oryzae* pv. *oryzae*. *FEMS Microbiol Lett* 259: 133-141
- 763 Furutani A, Takaoka M, Sanada H, Noguchi Y, Oku T, Tsuno K, Ochiai H, Tsuge S
764 (2009) Identification of novel type III secretion effectors in *Xanthomonas oryzae*
765 pv. *oryzae*. *Mol Plant Microbe Interact* 22: 96-106
- 766 Granier C, Vile D (2014) Phenotyping and beyond: modelling the relationships between
767 traits. *Curr Opin Plant Biol* 18C: 96-102
- 768 Green JM, Appel H, Rehrig EM, Harnsomburana J, Chung J-F, Balint-Kurti P, Shyu C-R
769 (2012) PhenoPhyte: a flexible affordable method to quantify 2D phenotypes from
770 imagery. *Plant Methods* 8: 45
- 771 Hothorn T, Bretz F, Westfall P (2008) Simultaneous inference in general parametric
772 models. *Biometrical J* 50: 346-363
- 773 Jalan N, Kumar D, Andrade MO, Yu F, Jones JB, Graham JH, White FF, Setubal JC,
774 Wang N (2013) Comparative genomic and transcriptome analyses of pathotypes
775 of *Xanthomonas citri* subsp. *citri* provide insights into mechanisms of bacterial
776 virulence and host range. *BMC Genomics* 14: 551

- 777 Kapur IN, Sahoo PK, Wong AKC (1985) A new method for the gray-level picture
778 thresholding using the entropy of the histogram. *Comput Vision Graph* 29: 273-
779 285
- 780 Kearney B, Staskawicz BJ (1990) Widespread distribution and fitness contribution of
781 *Xanthomonas campestris* avirulence gene *avrBs2*. *Nature* 386: 385-386
- 782 Khan M, Subramaniam R, Desveaux D (2016) Of guards, decoys, baits and traps:
783 pathogen perception in plants by type III effector sensors. *Curr Opin Microbiol*
784 29: 49-55
- 785 Kvitko BH, Park DH, Velasquez AC, Wei CF, Russell AB, Martin GB, Schneider DJ,
786 Collmer A (2009) Deletions in the repertoire of *Pseudomonas syringae* pv. *tomato*
787 DC3000 type III secretion effector genes reveal functional overlap among
788 effectors. *PLOS Pathog* 5: e1000388
- 789 Lacombe S, Rougon-Cardoso A, Sherwood E, Peeters N, Dahlbeck D, van Esse HP,
790 Smoker M, Rallapalli G, Thomma BP, Staskawicz B, Jones JD, Zipfel C (2010)
791 Interfamily transfer of a plant pattern-recognition receptor confers broad-spectrum
792 bacterial resistance. *Nat Biotechnol* 28: 365-369
- 793 Lamari L (2008) Assess 2.0: image analysis software for plant disease quantification.
794 American Phytopathological Society, St. Paul, MN.
- 795 Lee M-C, Weng S-F, Tseng Y-H (2003) Flagellin gene *fliC* of *Xanthomonas campestris*
796 is upregulated by transcription factor Clp. *Biochem Biophys Res Comm* 307: 647-
797 652
- 798 Lenth R (2015) lsmeans: least-squares means. R package version 2.20-23.
799 <http://CRAN.R-project.org/package=lsmeans>
- 800 Leucker M, Mahlein AK, Steiner U, Oerke EC (2016) Improvement of lesion
801 phenotyping in *Cercospora beticola*-sugar beet interaction by hyperspectral
802 imaging. *Phytopathology* 106: 177-184
- 803 Li B, Hulin MT, Brain P, Mansfield JW, Jackson RW, Harrison RJ (2015) Rapid,
804 automated detection of stem canker symptoms in woody perennials using artificial
805 neural network analysis. *Plant Methods* 11: 57
- 806 Li S, Wang Y, Wang S, Fang A, Wang J, Liu L, Zhang K, Mao Y, Sun W (2015) The
807 type III effector AvrBs2 in *Xanthomonas oryzae* pv. *oryzicola* suppresses rice
808 immunity and promotes disease development. *Mol Plant Microbe Interact* 28:
809 869-880
- 810 Li T, Liu B, Spalding MH, Weeks DP, Yang B (2012) High-efficiency TALEN-based
811 gene editing produces disease-resistant rice. *Nat Biotechnol* 30: 390-392
- 812 Lindeberg M, Cunnac S, Collmer A (2012) *Pseudomonas syringae* type III effector
813 repertoires: last words in endless arguments. *Trends Microbiol* 20: 199-208
- 814 Liu X, Sun Y, Korner CJ, Du X, Vollmer ME, Pajerowska-Mukhtar KM (2015) Bacterial
815 leaf infiltration assay for fine characterization of plant defense responses using the
816 *Arabidopsis thaliana*-*Pseudomonas syringae* pathosystem. *J Vis Exp* 104: e53364
- 817 Logue CA, Peak IR, Beacham IR (2009) Facile construction of unmarked deletion
818 mutants in *Burkholderia pseudomallei* using *sacB* counter-selection in sucrose-
819 resistant and sucrose-sensitive isolates. *J Microbiol Methods* 76: 320-323
- 820 Lozano JC (1986) Cassava bacterial blight: a manageable disease. *Plant Disease* 70:
821 1089-1093

- 822 Macho AP, Zipfel C (2014) Plant PRRs and the activation of innate immune signaling.
823 Mol Cell 54: 263-272
- 824 Mahlein AK, Steiner U, Hillnhütter C, Dehne HW, Oerke EC (2012) Hyperspectral
825 imaging for small-scale analysis of symptoms caused by different sugar beet
826 diseases. Plant Methods 8: 3
- 827 Metz M, Dahlbeck D, Morales CQ, Al Sady B, Clark ET, Staskawicz BJ (2005) The
828 conserved *Xanthomonas campestris* pv. *vesicatoria* effector protein XopX is a
829 virulence factor and suppresses host defense in *Nicotiana benthamiana*. Plant J
830 41: 801-814
- 831 Meyer D, Lauber E, Roby D, Arlat M, Kroj T (2005) Optimization of pathogenicity
832 assays to study the *Arabidopsis thaliana*-*Xanthomonas campestris* pv. *campestris*
833 pathosystem. Mol Plant Pathol 6: 327-333
- 834 Pinheiro J, Bates D, DebRoy S, Sarkar D, R Core Team (2016) nlme: linear and
835 nonlinear mixed effects models. R package version 3.1-128. [http://CRAN.R-](http://CRAN.R-project.org/package=nlme)
836 [project.org/package=nlme](http://CRAN.R-project.org/package=nlme)
- 837 Poland JA, Nelson RJ (2011) In the eye of the beholder: the effect of rater variability and
838 different rating scales on QTL mapping. Phytopathology 101: 290-298
- 839 Potnis N, Krasileva K, Chow V, Almeida NF, Patil PB, Ryan RP, Sharlach M, Behlau F,
840 Dow JM, Momol MT, White FF, Preston JF, Vinatzer BA, Koebnik R, Setubal
841 JC, Norman DJ, Staskawicz BJ, Jones JB (2011) Comparative genomics reveals
842 diversity among xanthomonads infecting tomato and pepper. BMC Genomics 12:
843 146
- 844 R Core Team (2015) R: A language and environment for statistical computing. R
845 Foundation for Statistical Computing, Vienna, Austria URL [http://www.R-](http://www.R-project.org/)
846 [project.org/](http://www.R-project.org/)
- 847 Raza SE, Prince G, Clarkson JP, Rajpoot NM (2015) Automatic detection of diseased
848 tomato plants using thermal and stereo visible light images. PLOS One 10:
849 e0123262
- 850 Rousseau C, Belin E, Bove E, Rousseau D, Fabre F, Berruyer R, Guillaumès J, Manceau
851 C, Jacques MA, Boureau T (2013) High throughput quantitative phenotyping of
852 plant resistance using chlorophyll fluorescence image analysis. Plant Methods 9:
853 17
- 854 Roux B, Bolot S, Guy E, Denance N, Lautier M, Jardinaud MF, Fischer-Le Saux M,
855 Portier P, Jacques MA, Gagnevin L, Pruvost O, Lauber E, Arlat M, Carrere S,
856 Koebnik R, Noel LD (2015) Genomics and transcriptomics of *Xanthomonas*
857 *campestris* species challenge the concept of core type III effectome. BMC
858 Genomics 16: 975
- 859 Schindelin J, Arganda-Carreras I, Frise E, Kaynig V, Longair M, Pietzsch T, Preibisch S,
860 Rueden C, Saalfeld S, Schmid B, Tinevez JY, White DJ, Hartenstein V, Eliceiri
861 K, Tomancak P, Cardona A (2012) Fiji: an open-source platform for biological-
862 image analysis. Nat Methods 9: 676-682
- 863 Schindelin J, Rueden CT, Hiner MC, Eliceiri KW (2015) The ImageJ ecosystem: An
864 open platform for biomedical image analysis. Mol Reprod Dev 82: 518-529
- 865 Schoonbeek HJ, Wang HH, Stefanato FL, Craze M, Bowden S, Wallington E, Zipfel C,
866 Ridout CJ (2015) Arabidopsis EF-Tu receptor enhances bacterial disease
867 resistance in transgenic wheat. New Phytol 206: 606-613

- 868 Schornack S, Moscou MJ, Ward ER, Horvath DM (2013) Engineering plant disease
869 resistance based on TAL effectors. *Annu Rev Phytopathol* 51: 383-406
- 870 Schulze S, Kay S, Buttner D, Egler M, Eschen-Lippold L, Hause G, Kruger A, Lee J,
871 Muller O, Scheel D, Szczeny R, Thieme F, Bonas U (2012) Analysis of new type
872 III effectors from *Xanthomonas* uncovers XopB and XopS as suppressors of plant
873 immunity. *New Phytol* 195: 894-911
- 874 Sinha D, Gupta MK, Patel HK, Ranjan A, Sonti RV (2013) Cell wall degrading enzyme
875 induced rice innate immune responses are suppressed by the type 3 secretion
876 system effectors XopN, XopQ, XopX and XopZ of *Xanthomonas oryzae* pv.
877 *oryzae*. *PLOS One* 8: e75867
- 878 Stam R, Mantelin S, McLellan H, Thilliez G (2014) The role of effectors in nonhost
879 resistance to filamentous plant pathogens. *Front Plant Sci* 5: 582
- 880 Stork W, Kim JG, Mudgett MB (2015) Functional analysis of plant defense suppression
881 and activation by the *Xanthomonas* core type III effector XopX. *Mol Plant*
882 *Microbe Interact* 28: 180-194
- 883 Strauß T, van Poecke RMP, Strauß A, Römer P, Minsavage GV, Singh S, Wolf C, Strauß
884 A, Kim S, Lee H-A, Yeom SI, Parniske M, Stall RE, Jones JB, Choi D, Prins M,
885 Lahaye T (2012) RNA-seq pinpoints a *Xanthomonas* TAL-effector activated
886 resistance gene in a large-crop genome. *Proc Natl Acad Sci USA* 109: 19480-
887 19485
- 888 Tai T, Dahlbeck D, Clark ET, Gajiwala P, Paison R, Whalen MC, Stall RE, Staskawicz
889 BJ (1999) Expression of the *Bs2* pepper gene confers resistance to bacterial spot
890 disease in tomato. *Proc Natl Acad Sci USA* 96: 14153-14158
- 891 Teper D, Burstein D, Salomon D, Gershovitz M, Pupko T, Sessa G (2016) Identification
892 of novel *Xanthomonas euvesicatoria* type III effector proteins by a machine-
893 learning approach. *Mol Plant Pathol* 17: 398-411
- 894 Tian F, Yu C, Li H, Wu X, Li B, Chen H, Wu M, He C (2015) Alternative sigma factor
895 RpoN2 is required for flagellar motility and full virulence of *Xanthomonas oryzae*
896 pv. *oryzae*. *Microbiol Res* 170: 177-183
- 897 Tornero P, Dangl JL (2001) A high-throughput method for quantifying growth of
898 phytopathogenic bacteria in *Arabidopsis thaliana*. *Plant J* 28: 475-481
- 899 Tripathi JN, Lorenzen J, Bahar O, Ronald P, Tripathi L (2014) Transgenic expression of
900 the rice *Xa21* pattern-recognition receptor in banana (*Musa* sp.) confers resistance
901 to *Xanthomonas campestris* pv. *musacearum*. *Plant Biotechnol J* 12: 663-673
- 902 Wei HL, Chakravarthy S, Mathieu J, Helmann TC, Stodghill P, Swingle B, Martin GB,
903 Collmer A (2015) *Pseudomonas syringae* pv. *tomato* DC3000 type III secretion
904 effector polymutants reveal an interplay between HopAD1 and AvrPtoB. *Cell*
905 *Host Microbe* 17: 752-762
- 906 Whalen MC, Innes RW, Bent AF, Staskawicz BJ (1991) Identification of *Pseudomonas*
907 *syringae* pathogens of *Arabidopsis* and a bacterial locus determining avirulence
908 on both *Arabidopsis* and soybean. *Plant Cell* 3: 49-59
- 909 White FF, Potnis N, Jones JB, Koebnik R (2009) The type III effectors of *Xanthomonas*.
910 *Mol Plant Pathol* 10: 749-766
- 911 Wickham H (2007) Reshaping Data with the reshape package. *Journal of Stat Softw* 21:
912 1-20. URL <http://www.jstatsoft.org/v21/i12/>
- 913 Wickham H (2009) ggplot2: elegant graphics for data analysis, Springer New York

- 914 Wickham H (2011) The split-apply-combine strategy for data analysis. *Journal of Stat*
915 *Softw* 40: 1-29. URL <http://www.jstatsoft.org/v40/i01/>
- 916 Wickham H (2015) scales: scale functions for visualization. R package version 0.3.0.
917 <http://CRAN.R-project.org/package=scales>.
- 918 Win J, Chaparro-Garcia A, Belhaj K, Saunders DG, Yoshida K, Dong S, Schornack S,
919 Zipfel C, Robatzek S, Hogenhout SA, Kamoun S (2012) Effector biology of
920 plant-associated organisms: concepts and perspectives. *Cold Spring Harb Symp*
921 *Quant Biol* 77: 235-247
- 922 Xie W, Yu K, Pauls KP, Navabi A (2012) Application of image analysis in studies of
923 quantitative disease resistance, exemplified using common bacterial blight-
924 common bean pathosystem. *Phytopathology* 102: 434-442
- 925 Xie Y (2015) knitr: a general-purpose package for dynamic report generation in R. R
926 package version 1.11.
- 927 Xu X, Miller SA, Baysal-Gurel F, Gartemann KH, Eichenlaub R, Rajashekara G (2010)
928 Bioluminescence imaging of *Clavibacter michiganensis* subsp. *michiganensis*
929 infection of tomato seeds and plants. *Appl Environ Microbiol* 76: 3978-3988
- 930 Zaman-Allah M, Vergara O, Araus JL, Tarekegne A, Magorokosho C, Zarco-Tejada PJ,
931 Hornero A, Alba AH, Das B, Craufurd P, Olsen M, Prasanna BM, Cairns J (2015)
932 Unmanned aerial platform-based multi-spectral imaging for field phenotyping of
933 maize. *Plant Methods* 11: 35
- 934 Zhao B, Dahlbeck D, Krasileva KV, Fong RW, Staskawicz BJ (2011) Computational and
935 biochemical analysis of the *Xanthomonas* effector AvrBs2 and its role in the
936 modulation of *Xanthomonas* type three effector delivery. *PLOS Pathog* 7:
937 e1002408
- 938 Zhao B, Lin X, Poland J, Trick H, Leach J, Hulbert S (2005) A maize resistance gene
939 functions against bacterial streak disease in rice. *Proc Natl Acad Sci USA* 102:
940 15383-15388
- 941

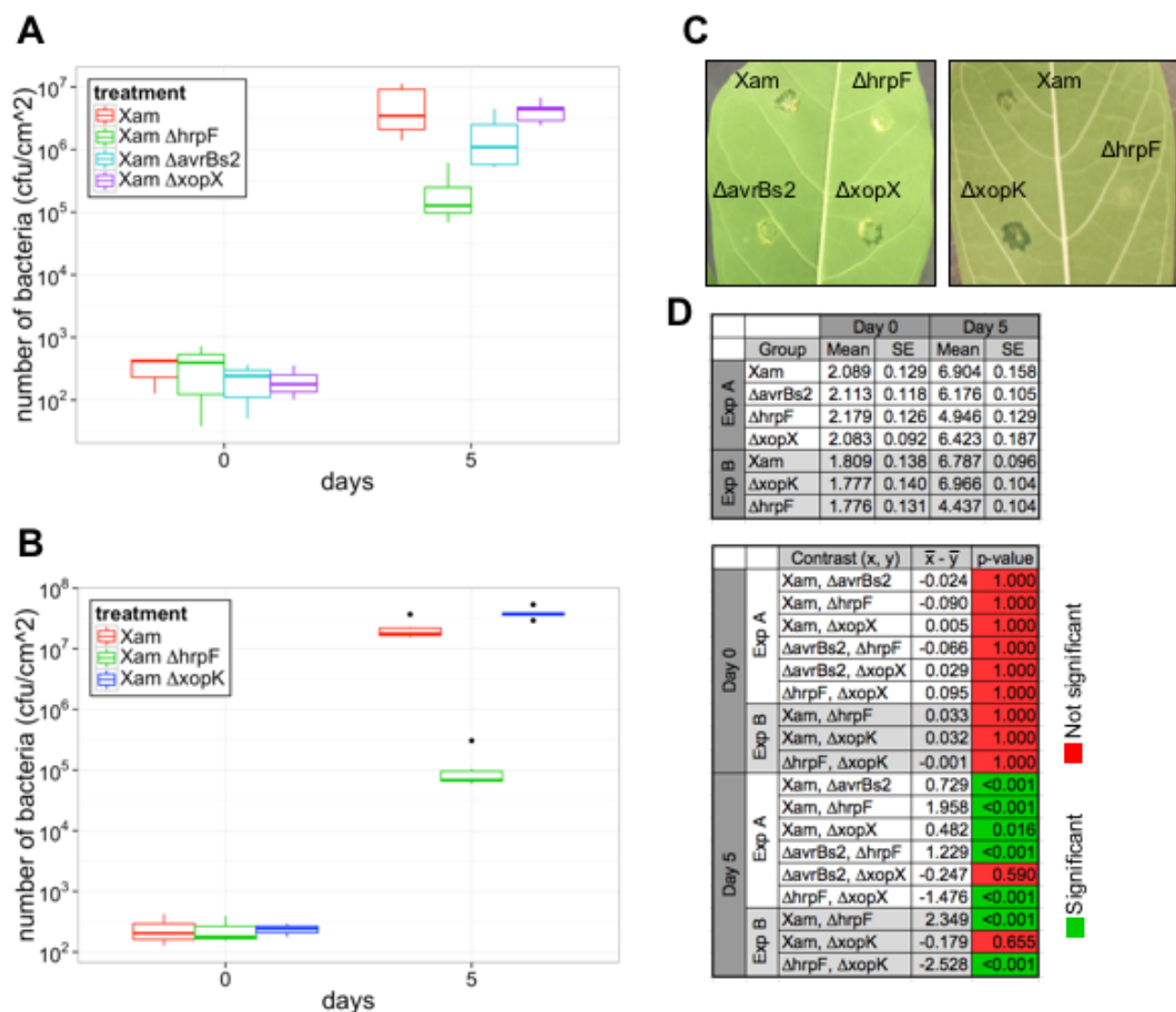


Figure 1. Disease symptom development and growth levels for *Xam* type III effector (T3E) mutants in cassava. A-B, Growth levels of *Xam* wild-type, Δ hrpF, Δ avrBs2, Δ xopX, and Δ xopK mutants following syringe infiltration in leaves ($OD_{600} = 0.0001$). Median, first and third quartiles are shown. The whiskers extend to the highest and lowest data point falling within $1.5 \times IQR$ (interquartile range). Dots represent outliers that fall outside $1.5 \times IQR$. Each experiment was repeated three additional times (see Supplemental Fig. S1). C, Comparison of disease symptoms caused by T3E mutants on leaves at 6 days after syringe infiltration ($OD_{600} = 0.0001$). D, Results of generalized linear mixed model analysis, combining bacterial growth data from all replicate experiments. Combined estimated means and standard error (SE) are presented, as well as the difference between the means and p-values for each pairwise statistical contrast.

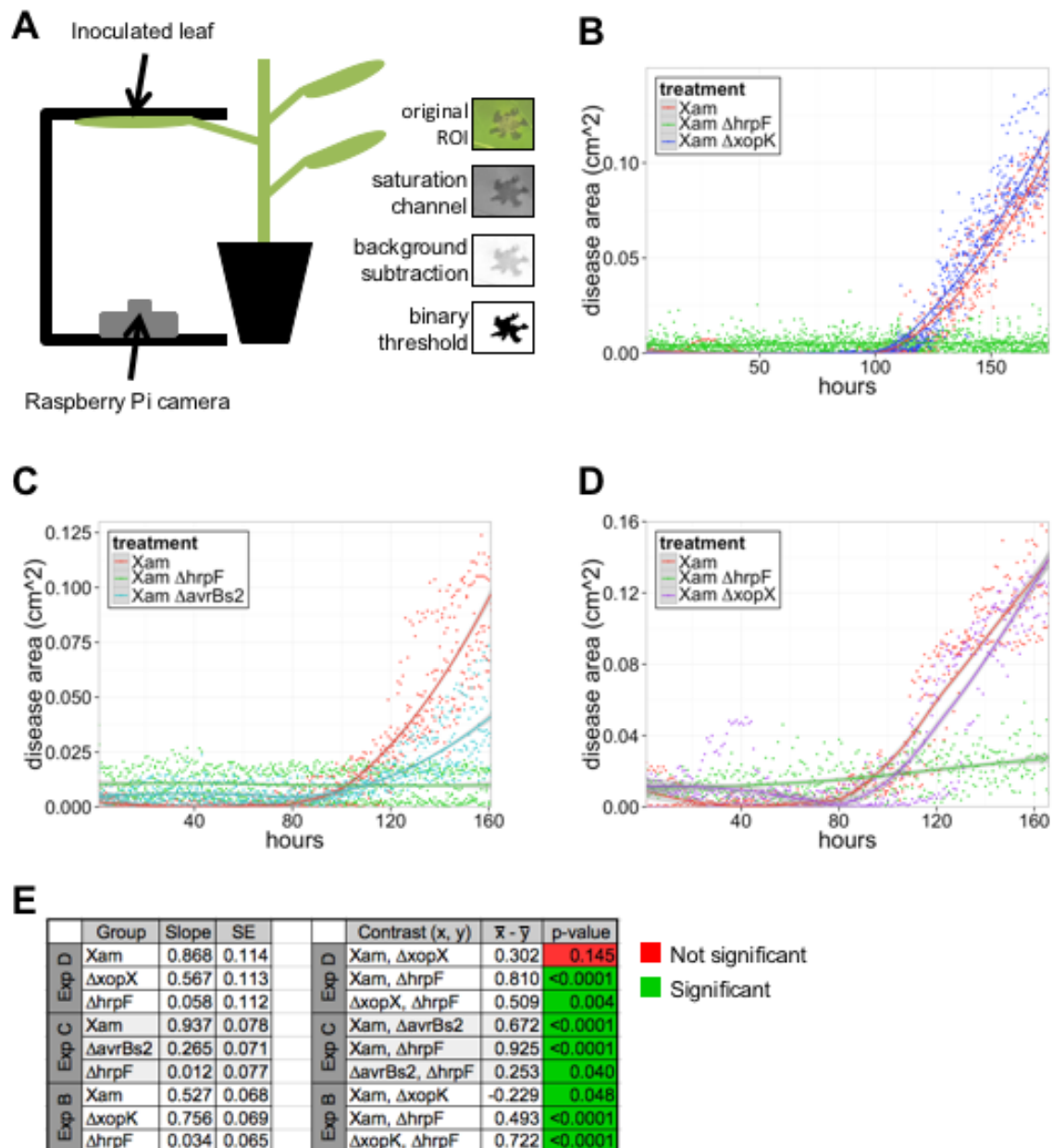


Figure 2. Quantification of disease symptoms caused by *Xam* on cassava leaves using imaging. A, Illustration of the imaging set-up. Leaves were syringe infiltrated with bacterial solutions ($OD_{600} = 0.001$) and taped to a black surface for imaging of the abaxial side of the leaf. Raspberry Pi microcomputer with attached camera collected images once per hour. Image analysis steps in ImageJ are shown and described in Materials and Methods. The number of black pixels was quantified to determine the area of disease. B-D, Quantification of water-soaking symptoms caused by the *Xam* wild-type strain and three mutants over time. Dots represent individual measurements determined from image analysis, and local regression fitted curves are plotted for each bacterial strain. Shaded areas represent the 95% confidence interval for each curve. The experiment was repeated three additional times with similar results (see Supplemental Fig. S3). E, Results of generalized linear mixed model analysis, combining data from all replicate experiments. Combined estimated slopes and standard error (SE) are presented, as well as p values for each pairwise statistical contrast.

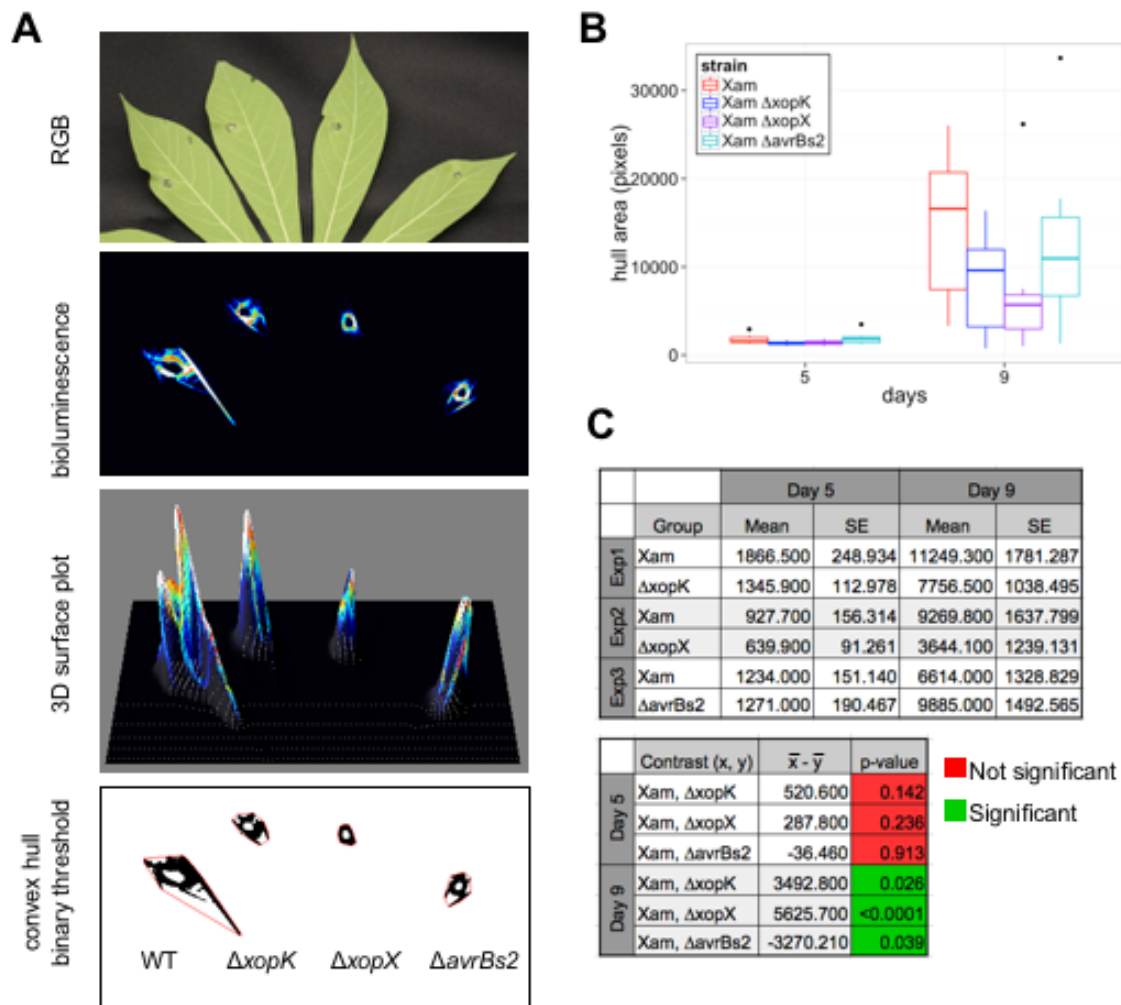


Figure 3. Bioluminescence imaging of *Xam* spread in cassava leaves. A, The bioluminescence reporter pLUX plasmid was introduced into *Xam* strains. Leaves were inoculated with bacterial solutions ($OD_{600} = 0.01$) using syringe infiltration. RGB images of inoculated leaves reveal symptom development. Bioluminescence was visualized in a dark chamber with a 5-10 min exposure. Image processing was performed with ImageJ to select the area of bioluminescence and the convex hull of the resulting shapes were analyzed. B, Representative quantification of convex hull for wildtype *Xam* and three mutants. Additional replicate experiments are shown in Supplemental Fig. S4. C, Results of generalized linear mixed model analysis of convex hull area, combining data from all replicate experiments. Combined estimated means and standard error (SE) are presented, as well as the difference between the means and the p-values for each pairwise statistical contrast.

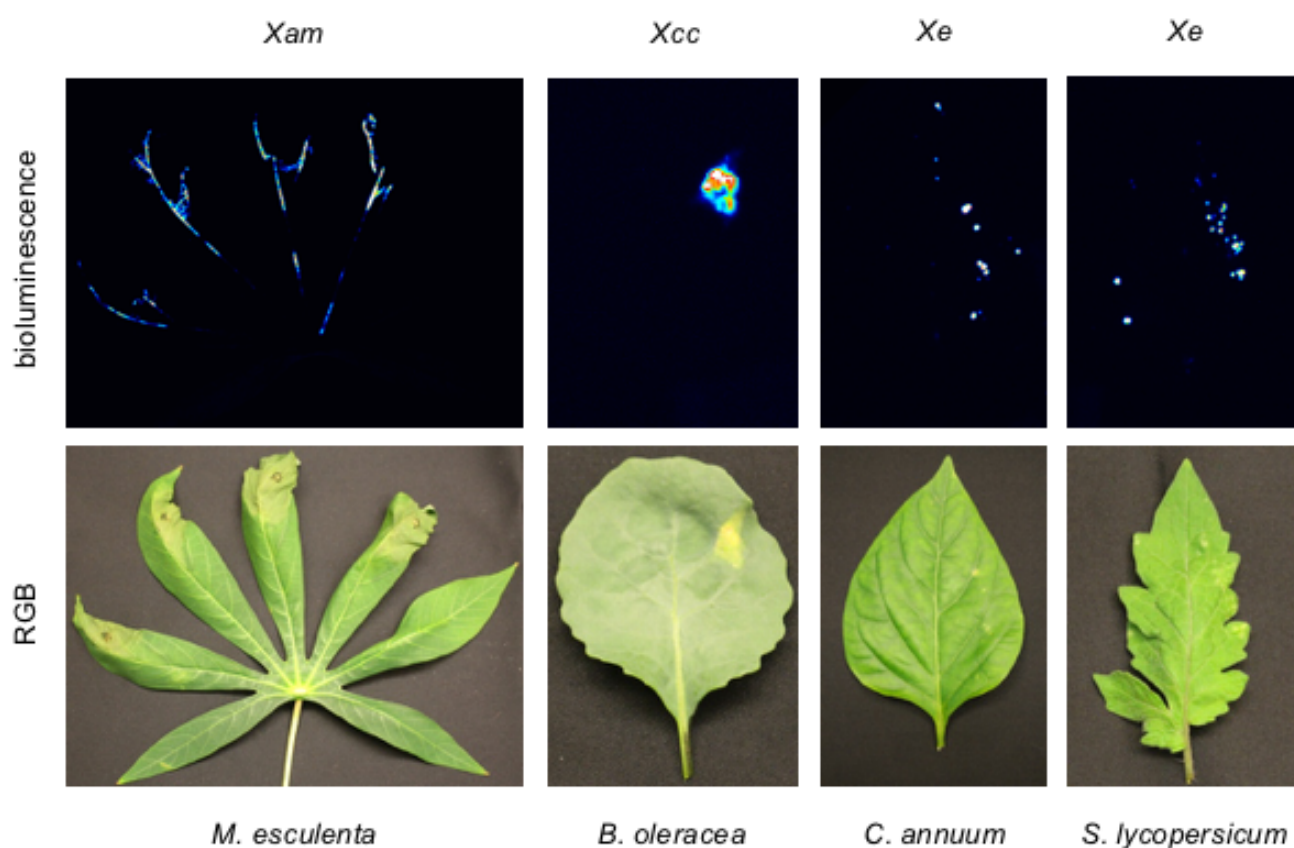


Figure 4. Comparison of vascular and leaf spot pathogens. *Xam* and *Xcc* were visualized following syringe inoculation ($OD_{600} = 0.01$) at 18 days post inoculation (dpi) and 12 dpi, respectively. Bacterial spot on pepper and tomato were visualized following dip inoculation ($OD_{600} = 0.5$) of *Xe* at 9 dpi.

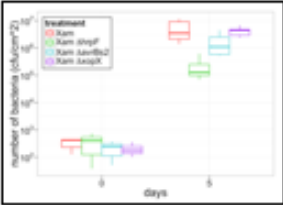
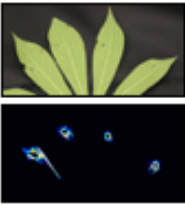
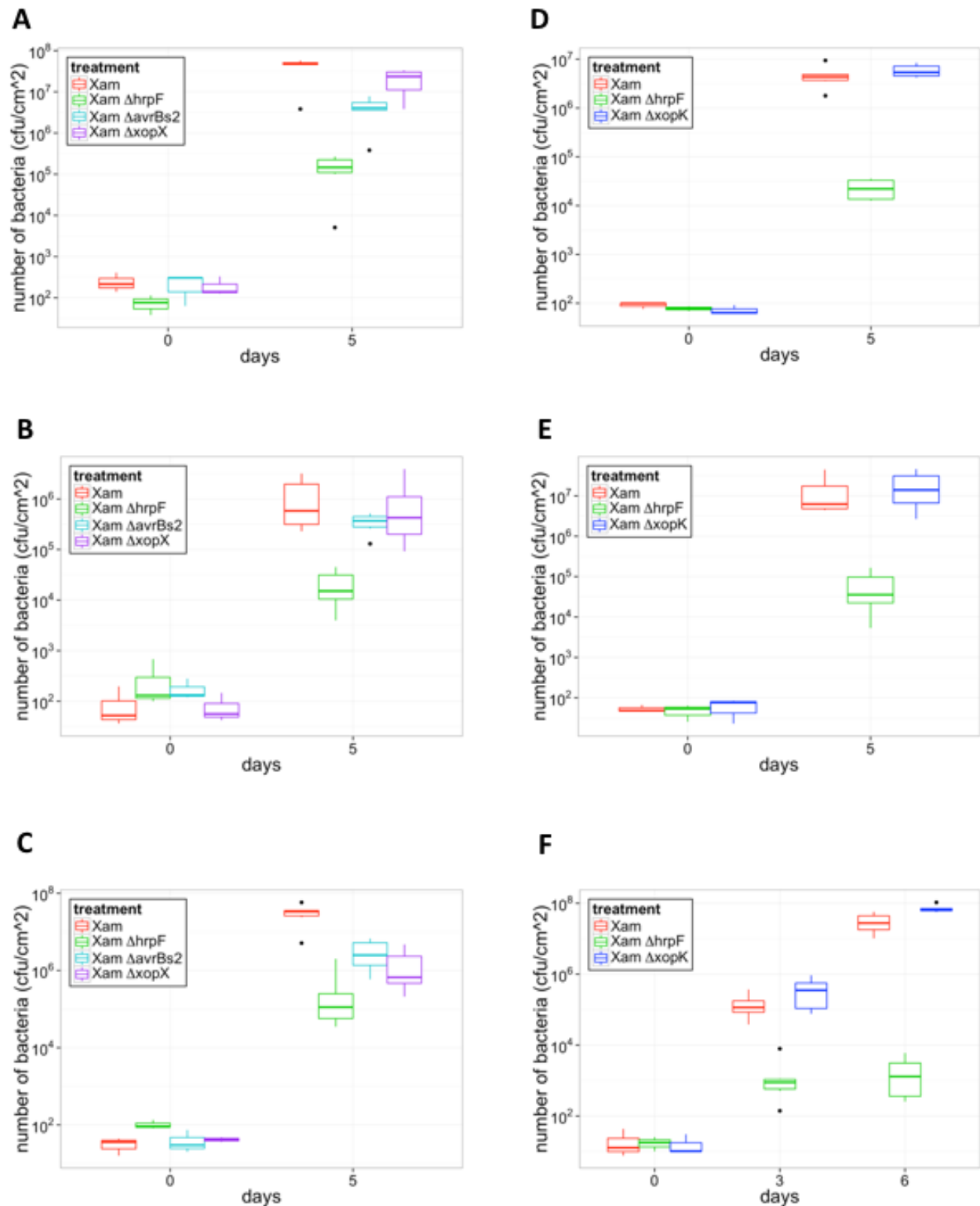
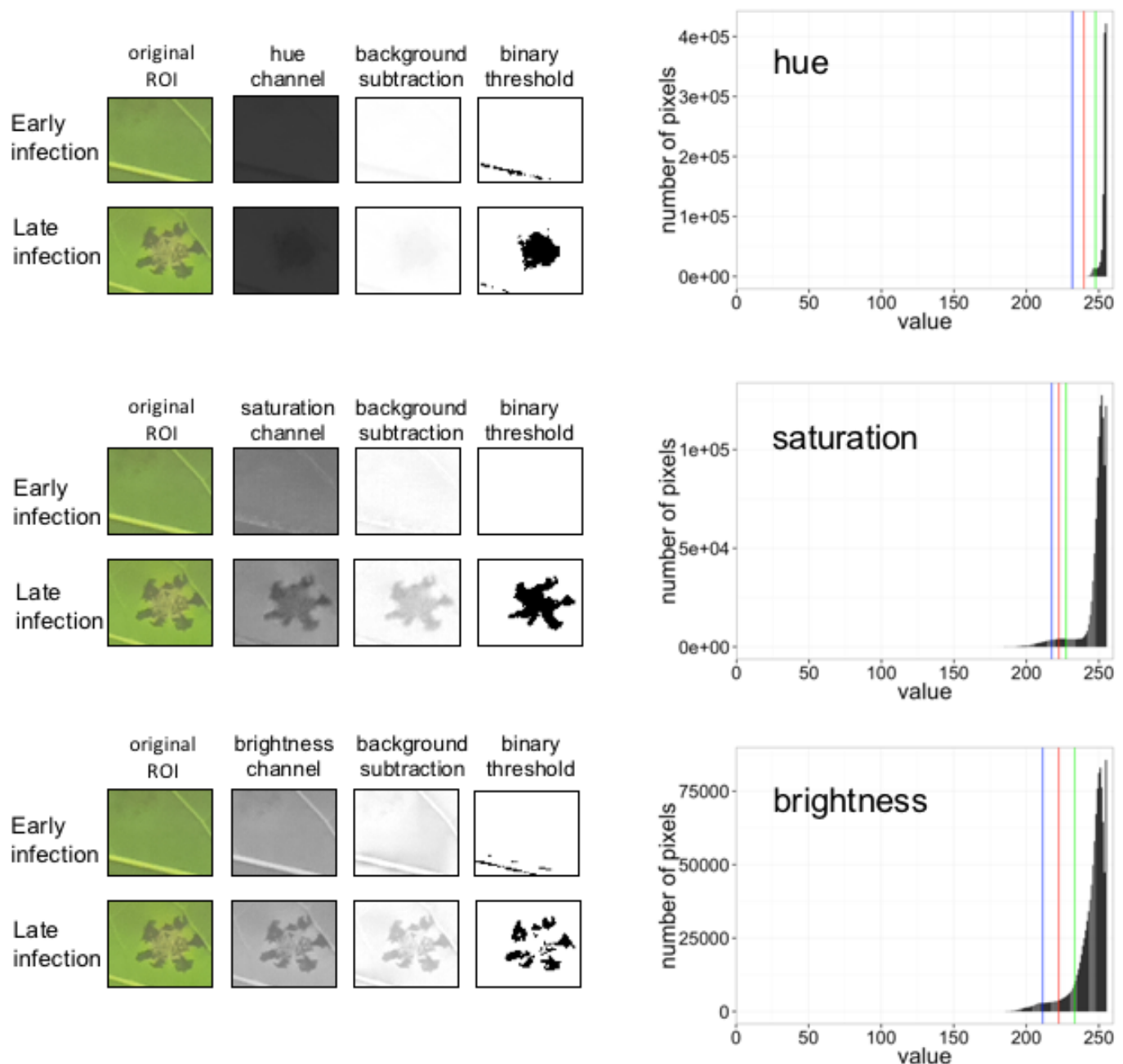
<i>Xam</i> T3E mutant	 Growth levels <i>in planta</i>	 Disease symptom progression	 Bacterial spread <i>in planta</i>	 <i>In vitro</i> motility
$\Delta xopK$	No change	Increased	Decreased	No change
$\Delta xopX$	Decreased	No change	Decreased	No change
$\Delta avrBs2$	Decreased	Decreased	Decreased	No change

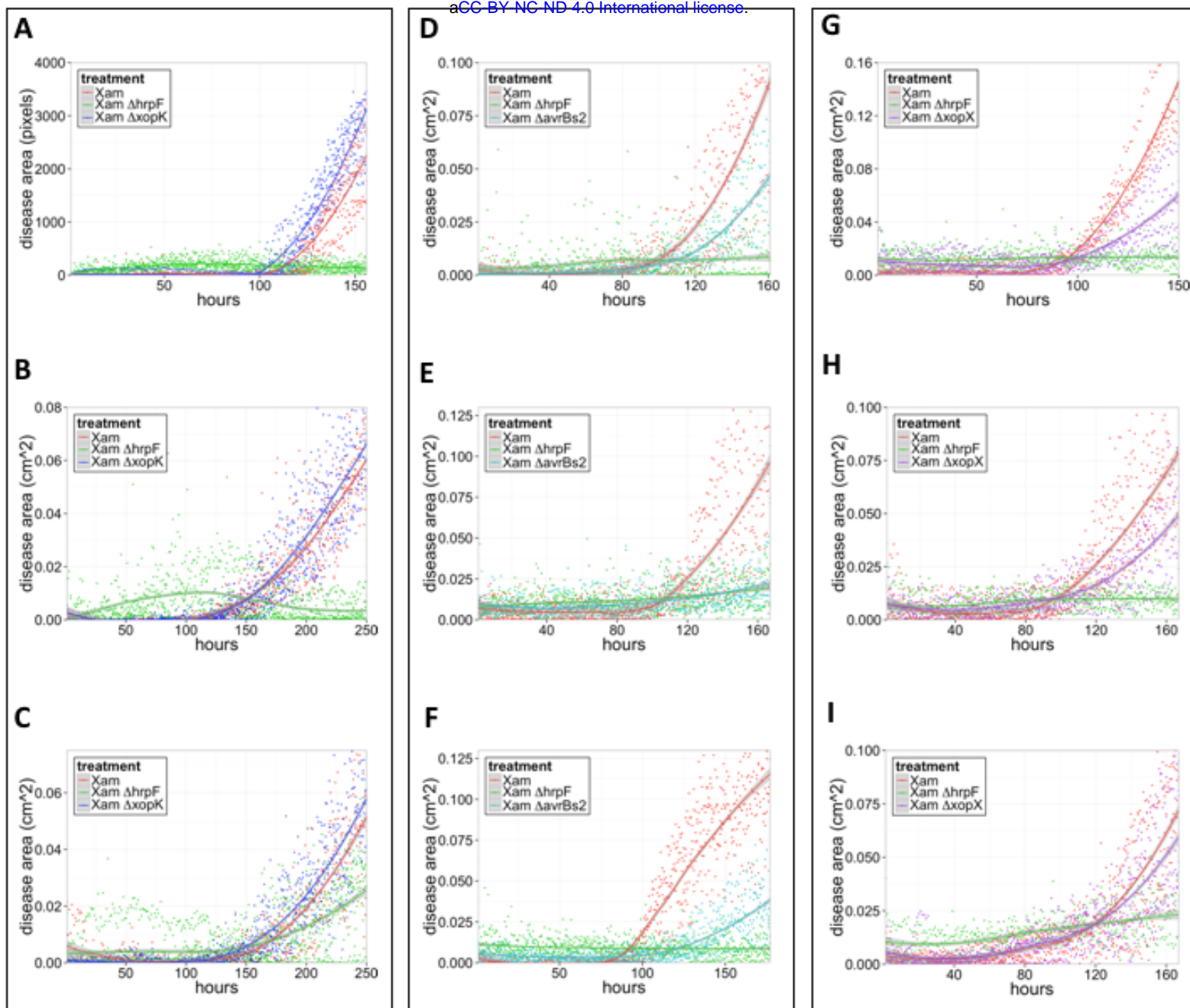
Figure 5. Summary for T3E mutant phenotypes as revealed by different phenotyping methods.



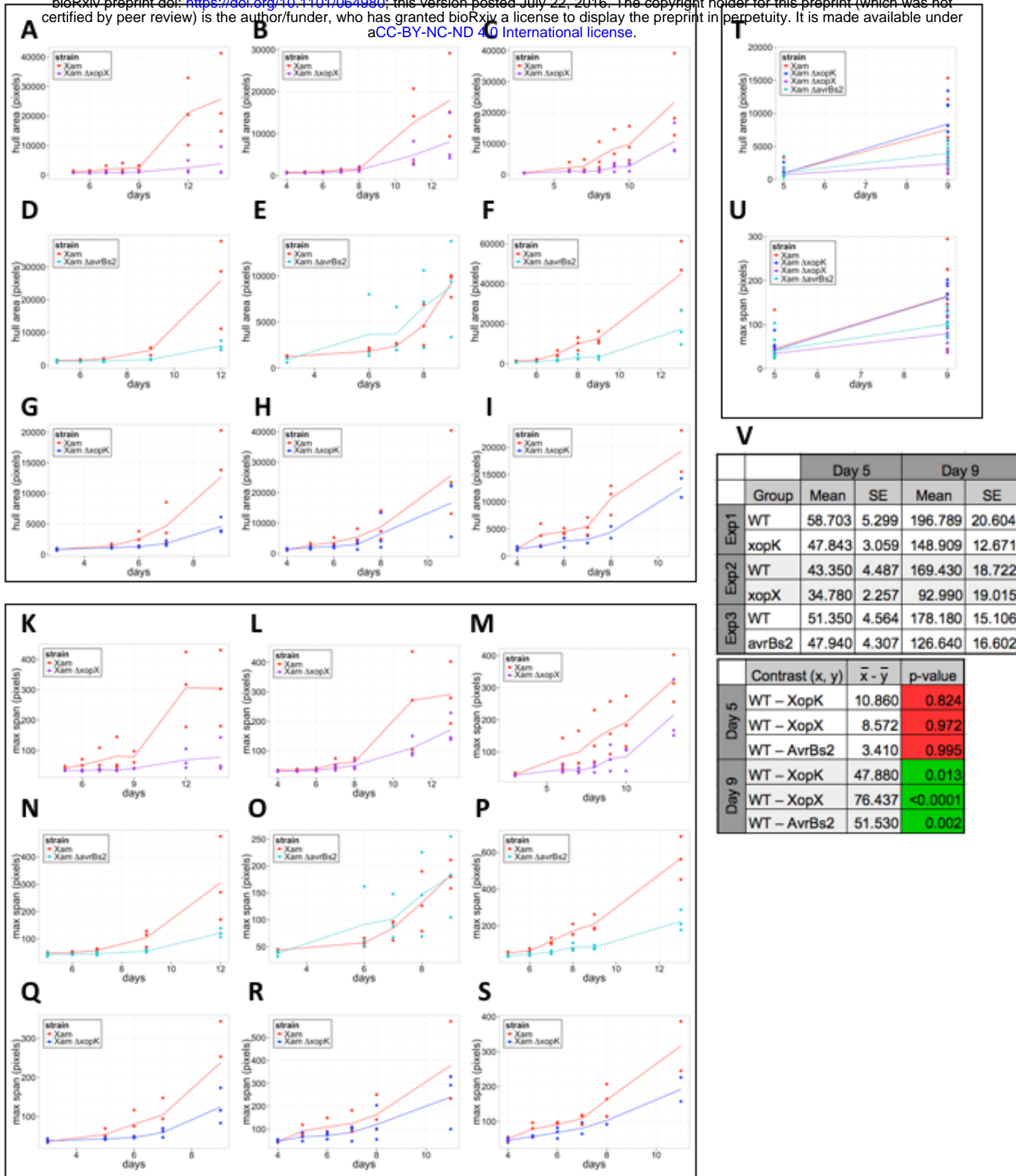
Supplemental Figure S1. Replicate experiments for analysis of *Xam* T3E mutant growth *in planta* shown in Figure 1. A-C, Three additional experiments to quantify growth levels of the *Xam* wild type strain, and the *Xam* $\Delta hrpF$, $\Delta avrBs2$, and $\Delta xopX$ mutants following syringe infiltration in leaves ($OD_{600} = 0.0001$). D-F, Three additional experiments to quantify growth levels of wild-type *Xam*, and the $\Delta hrpF$ and $\Delta xopK$ mutants following syringe infiltration in leaves ($OD_{600} = 0.0001$).



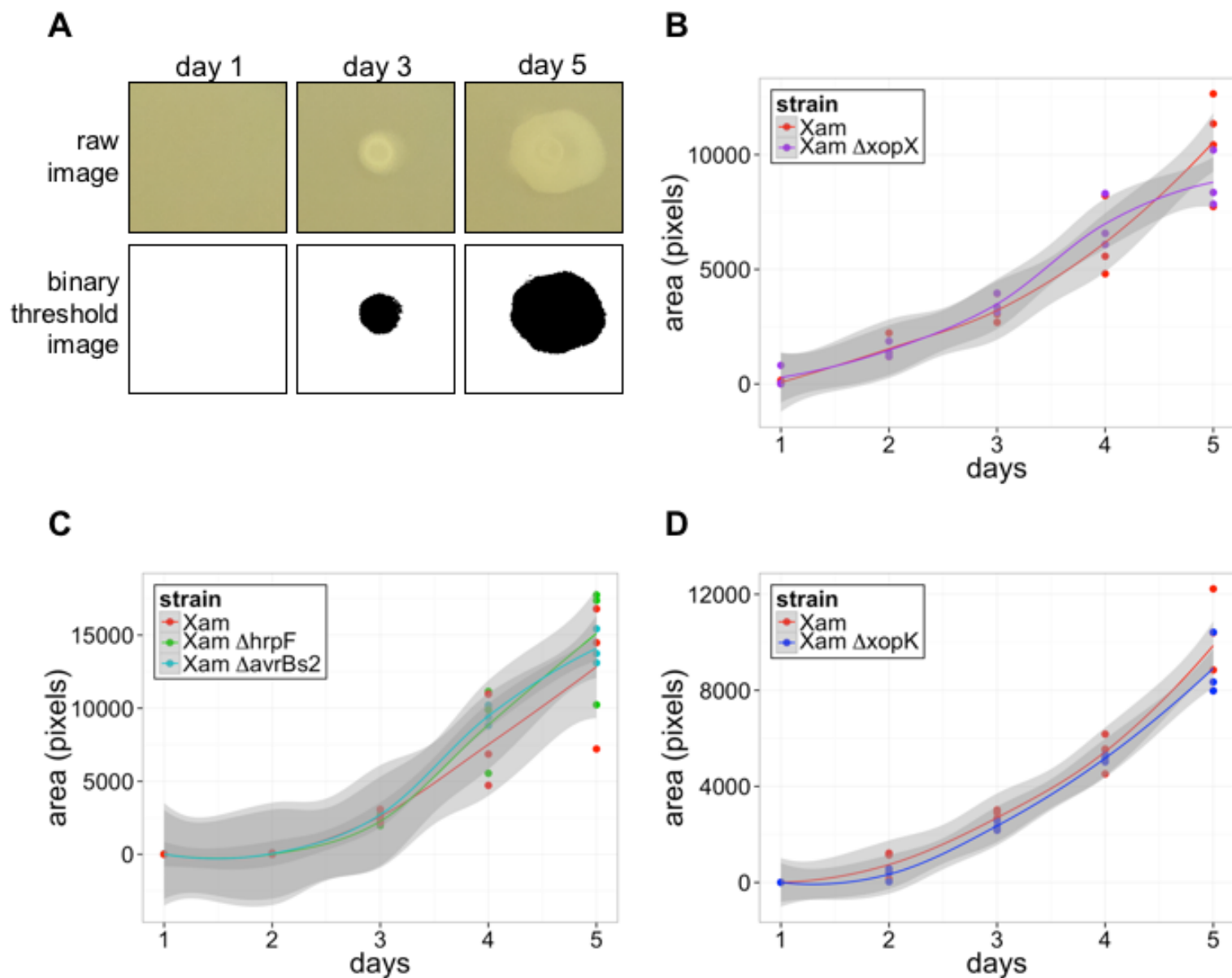
Supplemental Figure S2. Image analysis optimization for water-soaking disease symptoms caused by *Xam*. Following conversion of regions of interest (ROI) to hue-saturation-brightness (HSB) color space and background subtraction, the distributions of pixel values for each channel were examined. Disease symptoms are best represented by pixel values in the lower tail of the distribution for the saturation channel. A range of threshold values were applied to the images to create binary images, according to the formula $t = \mu - n\sigma$, where t = threshold, μ = mean saturation value for the image stack, and σ = standard deviation of saturation values for the image stack. Graphs show example thresholds where $n = 3$ (blue line), $n = 2.5$ (red line), and $n = 2$ (green line). The binary images on the right show the results of applying the $n = 3$ threshold.



Supplemental Figure S3. Three additional replicate experiments for analysis of water-soaking symptoms shown in Fig. 2. Dots represent individual measurements determined from image analysis, and local regression fitted curves are plotted for each bacterial strain. Shaded areas represent the 95% confidence interval for each curve. For the experiment shown in A, the image distances were not scaled to cm, so values are reported in pixels. Experiments shown in panels D-F and H-I were performed with cassava variety TME7.



Supplemental Figure S4. Replicate experiments for analysis of *Xam* spread in leaves using bioluminescence imaging shown in Fig. 3. Three additional experiments quantifying the convex hull area for the *Xam* $\Delta xopX$ (A-C), $\Delta avrBs2$ (D-F), and $\Delta xopK$ (G-I) mutants. Quantification of the maximum span across the convex hull for the same experiments (K-S). Quantification of the convex hull area (T) and maximum span (U) for a fourth replicate including the three mutants. Dots represent individual measurements; lines connect the mean at each time point. V, Results of generalized linear mixed model analysis for maximum span results, combining data from all replicate experiments. Combined estimated means and standard error (SE) are presented, as well as p values for each pairwise statistical contrast.



Supplemental Figure S5. *In vitro* motility of *Xam* T3E mutants. Bacteria were spotted in the center of plates containing NYG media with 0.25% agar. Images were taken of the plates over several days, and the area of bacterial spread was quantified using ImageJ. A, Example of binary thresholding used to select the area of bacterial spread from the images. B-D, Quantification of bacterial spread for the *Xam* T3E mutants, relative to the wild-type strain. Dots represent individual data points, and local regression fitted curves are plotted for each bacterial strain. Shaded areas represent the 95% confidence interval for each strain.

```
/* Author: Andrew Mutka, Donald Danforth Plant Science Center, St. Louis, MO
 *
 * ImageJ macro script to select and quantify the area of water-soaking disease
 * symptoms for regions of interest from images of inoculated leaves
 */
```

```
function ws_quant(input, output, filename) {
    open(input + filename);
    sourceTitle = getTitle();
    selectWindow(""+sourceTitle+"");
    //convert images to HSB color space and select the saturation channel
    run("HSB Stack");
    run("Split Channels");
    selectWindow("C1-"+sourceTitle+"");
    close();
    selectWindow("C3-"+sourceTitle+"");
    close();
    selectWindow("C2-"+sourceTitle+"");
    //subtract background from the images
    run("Subtract Background...", "rolling=50 light stack");
    //calculate the mean and standard deviation of saturation values from the image stack
    run("Set Measurements...", "mean standard redirect=C2-"+sourceTitle+" decimal=9");
    run("Statistics");
    selectWindow("Results");
    mean=getResult("Mean");
    stdDev=getResult("StdDev");
    //set n as a multiple of stdDev to calculate the desired threshold level
    n=3;
    threshold=mean-(n*stdDev);
    //print a log of threshold values used
    print(mean, stdDev, threshold);
    //apply the threshold to the image stack
    selectWindow("C2-"+sourceTitle+"");
    setAutoThreshold("Default");
    setThreshold(0, threshold);
    run("Convert to Mask", "method=Default background=Default");
    //save the binary images
    saveAs("Tiff", output + filename);
    //calculate the area of black pixels in the binary images
    run("Set Measurements...", "area redirect=["+sourceTitle+"] decimal=9");
    run("Analyze Particles...", "summarize stack");
    //save the results as a csv file
    saveAs("Results", output + filename + ".csv");
    close();
    run("Clear Results");
}
```

```
//set input/output variables based on directory containing images and desired output directory
input = "/Users/amatka/input/";
output = "/Users/amatka/output/";

//calculate threshold areas for each image stack in a directory
setBatchMode(true);
list = getFileList(input);
for (i = 0; i < list.length; i++)
    ws_quant(input, output, list[i]);
setBatchMode(false);
```

```

/*****
 * Author: Andrew Mutka, Donald Danforth Plant Science Center, St. Louis, MO
 *
 * ImageJ macro script to quantify bacterial spread on soft agar plates
 *
 *****/

function motility_quant(input, output, filename) {
    open(input + filename);
    sourceTitle = getTitle();
    selectWindow(""+sourceTitle+"");
    //convert to 8-bit grayscale images
    run("8-bit");
    //enhance contrast of the images
    run("Enhance Contrast...", "saturated=0.4 normalize process_all use");
    //create binary images using thresholding
    run("Auto Threshold", "method=MaxEntropy white stack use_stack_histogram");
    run("Despeckle", "stack");
    run("Invert", "stack");
    run("Convert to Mask", "stack");
    //save the binary images
    saveAs("Tiff", output + filename);
    //calculate the area of black pixels in the binary images
    run("Set Measurements...", "area redirect=["+sourceTitle+"] decimal=9");
    run("Analyze Particles...", "include summarize stack");
    //save the results as a csv file
    saveAs("Results", output + filename + ".csv");
    close();
}

//set input/output variables based on directory containing images and desired output directory
input = "/Users/anutka/input/";
output = "/Users/anutka/output/";

//calculate threshold area for each image stack in the directory
setBatchMode(true);
list = getFileList(input);
for (i = 0; i < list.length; i++)
    motility_quant(input, output, list[i]);
setBatchMode(false);
}
```